

Neutron Stars Merger Remnants

Sebastiano Bernuzzi

Received: date / Accepted: date

Abstract Binary neutron star mergers observations are a unique way to constrain fundamental physics and astrophysics at the extreme. The interpretation of gravitational-wave events and their electromagnetic counterparts crucially rely on general-relativistic models of the merger outcome and remnant properties. Quantitative models can be obtained only with numerical relativity simulations in 3+1 dimensions that include detailed input physics for the nuclear matter and weak interactions. This review summarizes our current understanding of the merger's remnant focusing on some of the aspects that are relevant for multimessenger observations.

Keywords Binary neutron star · mergers · remnants · gravitational-waves · numerical relativity

1 Introduction

The gravitational-wave GW170817 is compatible with a binary neutron star (BNS) inspiral of chirp mass $1.186(1)M_{\odot}$ [1, 2, 3]. Significant signal-to-noise ratio (SNR) is found in the range 30 to 600 Hz, roughly corresponding to the last thousand orbits to merger for an equal-mass binary with canonical mass $M \sim 2.8 M_{\odot}$. The matched-filtering analysis of GW170817 with waveform templates including tidal effects provided us with an estimate of the tidal polarizability parameter distributed around $\tilde{\Lambda} \sim 300$ and smaller than ~ 800 [4, 5, 6, 7]. LIGO-Virgo searches for short ($\lesssim 1$ s), intermediate ($\lesssim 500$ s) and long (days) postmerger transients from a neutron star (NS) remnant resulted in

S. Bernuzzi
Theoretisch-Physikalisches Institut
Friedrich-Schiller-Universitaet Jena
Max Wien Platz 1
D-07743 Jena, Germany
E-mail: sebastiano.bernuzzi@uni-jena.de

upper limits of more than one order of magnitude larger than those predicted by basic models of quasi-periodic sources [8, 9, 10, 11, 12]. Hence, the LIGO-Virgo detectors' sensitivity was not sufficient to detect a signal from the merger phase and the remnant, which lies in the kHz range [13]. A similar conclusion holds for the second BNS event, GW190425, that was detected at lower SNR than GW170817[14]. GW190425 has a chirp mass of $1.44(2) M_{\odot}$ and it is associated to the heaviest BNS source known to date.

In absence of a GW detection, the merger remnant can be inferred from the binary properties and from the interpretation of the electromagnetic counterparts based on the theoretical predictions given by numerical relativity (NR) simulations. The latter are the only method available to determine the merger outcome and to compute the GW signals from the remnants. This review summarizes the current understanding of merger remnants as determined by NR simulations during the last 20 years ¹ The presented results are key for the interpretation of future observations of multimessenger signals from BNS mergers.

Current numerical relativity methods applied to quasicircular mergers allows us to simulate tens of orbits before merger and the early postmerger phase for a timescale of several dynamical periods. The NSs in the orbital phase are well described by zero-temperature matter in beta-equilibrium with maximum density about twice the nuclear saturation density $\rho_{\text{NS}} \sim 2 - 3\rho_0$ ($\rho_0 \simeq 2.3 \times 10^{14}$ gcc). Electromagnetic fields are not expected to significantly affect the mass dynamics. Thus, general-relativistic simulations with perfect fluid matter are believed to faithfully reproduce this dynamical phase. The latter can be characterized in terms of the binary masses (and spins), and one tidal polarizability parameter, as described in Sec. 2. At the end of the chirp signal, about 3-4% of the initial gravitational mass is radiated in GWs and the binary merges at typical GW frequencies $\sim 1 - 2$ kHz.

Binary NS mergers result in the formation of a compact central object, either a NS or a black hole (BH), eventually surrounded by an accretion disc [15, 16, 17, 18]. The remnant can be characterized in first approximation by the NS masses and by the softness of the (unknown) zero-temperature equation of state (EOS), in particular by the maximum sustained mass, $M_{\text{max}}^{\text{TOV}}$ [19, 20]. Binary remnants with total mass significantly larger than $M_{\text{max}}^{\text{TOV}}$ cannot be sustained by the EOS pressure and by the centrifugal support of their rotations. Thus, the remnant promptly collapses to a BH during its formation. A precise definition of prompt BH collapse and the phenomenology inferred from the simulations are discussed in Sec. 3.

If the remnant does not promptly collapse, its early evolution is determined by GW emission and by a characteristic luminous GW transient emitted at frequencies about twice the fluid's rotation, i.e. $\sim 2 - 4$ kHz [16, 21, 22, 23, 24, 25]. Matter in NS remnants is compressed and heated up to extreme densities and temperatures. The baryon mass density can reach $\rho_{\text{rem}} \sim 1.5 - 2\rho_{\text{NS}} \sim 3 - 6\rho_0$

¹ This review reflects the views of the author who aimed at a brief but updated overview avoiding a more complete historical perspective.

and temperatures $\gtrsim 50$ MeV [26, 27]. The NS remnant can either collapse to BH after a “short life” on the dynamical timescales determined by the rotation, or settle to an axisymmetric equilibrium configuration on longer timescales. The black holes that can be produced in BNS mergers are discussed in Sec. 4.

After the dynamical, GW-driven, phase the angular momentum of the NS remnant at formation is well above the Keplerian (mass-shedding) limit of an equilibrium zero-temperature beta-equilibrated rigidly-rotating configuration with the same baryon mass [28]. Also, the remnant has gravitational mass in excess with respect to those equilibrium configurations. Thus, it is far from equilibrium and its long-term evolution is determined by the energy and angular momentum evolution due to magnetohydrodynamical and weak interactions in the fluid as well as GW emission [29, 30, 31, 32]. Neutron-star remnants and their evolutionary phases are discussed in Sec. 5.

A key dynamical feature for GW counterparts is the formation of remnant discs [33, 34, 35, 36, 37, 35]. Discs of masses $\sim 0.1 M_\odot$ can form in BNS remnant if the matter acquires sufficient rotational (centrifugal) support during merger. The initial composition and extension of a remnant disc is dependent on whether the central object is a NS or a BH. The disc evolution starts with a phase of rapid accretion, but is afterwards determined by a combination of the gravitational pull, the neutrino cooling and the expansion due to viscous processes [38, 39, 40, 41, 42, 29]. The properties of remnant discs are discussed in Sec. 6.

Mass ejecta from mergers are a key astrophysical site for heavy-element production via the r-process [43, 44, 45, 46, 47, 48]. The associated kilonova signal was observed after GW170817 and, because of its quasi-isotropic character, it is considered to be the most promising EM counterpart for future events [49, 50, 51, 52, 53]. During the last orbits a mass of $\sim 10^{-4} - 10^{-2} M_\odot$ of neutron rich material is expelled on dynamical timescales [54, 55, 56, 45, 30]. The remnant, however, can unbind an even larger amount of material by winds powered by different mechanisms [57, 58, 59, 42, 60]. These ejection mechanisms and NR-based estimates of ejecta masses and composition are reviewed in Sec. 7.

Appendix A summarizes the main input physics and numerical techniques employed for the NR simulations.

We use geometric units $G = c = 1$ if units are not explicitly indicated.

2 Merger dynamics

The inspiral BNS dynamics differ from the binary black hole one because of the tidal interactions between the NSs. Tidal interactions in the post-Newtonian formalism for self-gravitating and deformable bodies are formulated using a multi-chart approach in which the tidal response of a NS due to the external gravitational field of the companion (inner problem) is matched to an outer problem for the description of the orbital dynamics and radiation [62, 63, 64, 65,

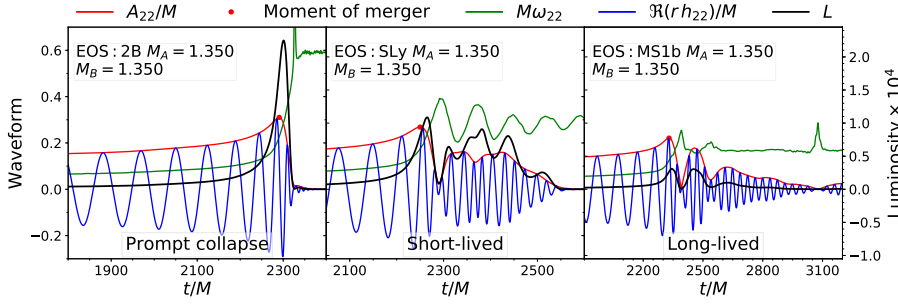


Fig. 1 Gravitational-waveforms for representative equal-mass irrotational mergers. The figure shows the evolution of amplitude, frequency and real part of the $(2, 2)$ multipole of the GW strain and luminosity. From left to right: prompt collapse, short-lived, and long-lived and stable remnant. Figure adapted from [61].

66]. In the local frame of body A , the mass M_L^A multipole moments² are related to the external gravitoelectric moments G_L^A by $M_L^A = \mu_\ell^A G_L^A$ where $L = i_1 \dots i_\ell$ is a multi-index. Analogously to the electric polarizability of a charge distribution, the coefficients μ_ℓ quantify the distortion of the mass distribution under the external field. They are often substituted by the dimensionless relativistic Love numbers obtained by normalizing with the proper power of the NS radius,

$$k_\ell^A := \frac{(2\ell - 1)!!}{2} \frac{G\mu_\ell^A}{R_A^{2\ell+1}}. \quad (1)$$

The practical calculation of the Love numbers reduces to the solution of stationary perturbations of spherical relativistic stars [62, 67, 68, 69]. The Love numbers are thus dependent on the EOS employed for constructing the equilibrium NS and on the NS compactness, $C_A = GM_A/(c^2 R_A)$. In the following we will make use exclusively of the quadrupolar *tidal polarizability parameters* defined as [70, 66]

$$\Lambda_A := \frac{2}{3} k_2^A \left(\frac{GM_A}{R_A c^2} \right)^5. \quad (2)$$

The two-body relative dynamics in the weak field regime is described by the Newtonian Hamiltonian with a tidal term in the potential [66, 4],

$$H \simeq \frac{\mu}{2} p^2 + \frac{\mu}{2} \left(-\frac{2GM}{c^2 r} + \dots - \frac{\kappa_2^T}{r^6} \right). \quad (3)$$

where μ is the reduced mass of the binary. The coupling constant κ_2^T is defined as

$$\kappa_2^T := \frac{3}{2} \left[\Lambda_2^A \left(\frac{M_A}{M} \right)^4 \frac{M_B}{M} + (A \leftrightarrow B) \right], \quad (4)$$

² There exists also spin multipole moments and gravitomagnetic tidal moment. The discussion here is simplified.

and parametrizes at leading (Newtonian) order the tidal interactions in the binary. The formula above indicates that tidal interactions are attractive and short-range ³ The effect of tidal interactions in the inspiral is illustrated by the (modified) Kepler law [66],

$$\Omega^2 r^3 = GM \left[1 + 12 \frac{M_A}{M_B} \frac{R_A^5}{r^5} k_2^A + (A \leftrightarrow B) \right]. \quad (5)$$

At a given radius the frequency is higher if the tidal interactions are present. Thus, the motion is accelerated by tidal effects and the system merges earlier and at a lower frequency. We shall see that, while the details of tidal interactions during merger can be quantified only by general relativistic hydrodynamical simulations, these basic results are key to characterize the merger data from the simulations. Note the tidal parameter [5]

$$\tilde{\Lambda} := \frac{16}{13} \frac{(M_A + 12M_B)M_A^4}{M^5} \Lambda_A + (A \leftrightarrow B), \quad (6)$$

is sometimes used to parametrize tides instead of κ_2^T . Although not the same quantity, $\tilde{\Lambda}$ and κ_2^T will be used here for the same purposes. The ranges for BNS are $\kappa_2^T \approx (20, 500)$ and $\tilde{\Lambda} \approx (50, 2000)$. Softer EOS, larger masses and higher mass-ratios result in smaller values of κ_2^T (or $\tilde{\Lambda}$). In what follows we discuss an effective characterization of the merger properties relevant for the later discussion on the merger remnant.

The BNS dynamics in numerical relativity is usually studied by considering the gravitational radiation computed in the simulations. The latter is extracted from coordinate spheres at finite radii R and eventually extrapolated at null-infinity. Simulations resolve the first modes of the multipolar decomposition,

$$h_+ - ih_\times = \sum_{\ell=2}^{\infty} \sum_{m=-\ell}^{\ell} R h_{\ell m}(t) {}^{-2}Y_{\ell m}(\theta, \varphi) \approx R h_{22}(t) {}^{-2}Y_{22}(\theta, \varphi) + c.c., \quad (7)$$

where ${}^{-2}Y_{\ell m}$ are the spin-weighted $s = -2$ spherical harmonics. Examples of circular merger gravitational-waves are shown in Fig. 1 together with the instantaneous GW frequency and luminosity. All the waveforms show the chirp behaviour known from the post-Newtonian formalism that terminates at a characteristic amplitude peak, the time of which is sometimes referred as *moment of merger* (and distinguished from the merger process). The moment of merger marks the end of the chirp signal. Note the luminosity peak is delayed with respect to the amplitude peak.

A gauge invariant way to characterize the BNS dynamics using simulation data is to consider the reduced binding energy and angular momentum of the

³ The dependency on the orbital separation follows immediately from the Lagrangian at leading order $L \approx +\mu_2 G_{ab} G^{ab}$ and the general property $G_L \propto \partial_L u \propto r^{\ell+1}$.

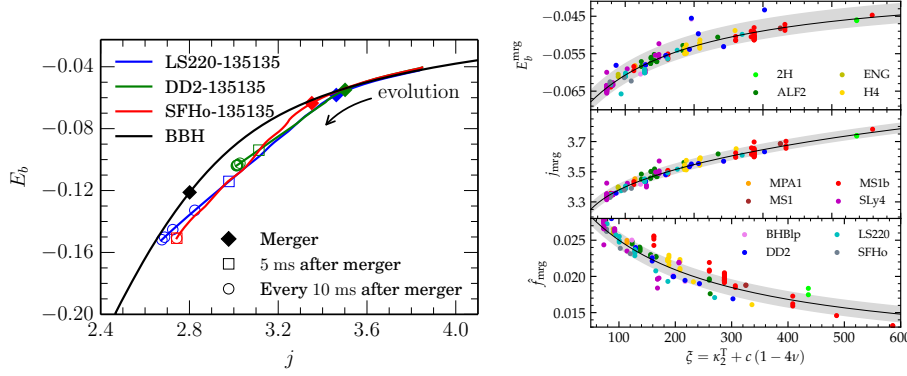


Fig. 2 Energetics of BNS mergers and quasiuniversal (EOS-independent) relations at the moment of merger. Left: Evolution of the reduced binding energy and angular momentum Eq. 8-9 for representative models and comparison to the binary black hole case. The moment of merger is marked by a squared black bullet, subsequent times are marked with empty bullets. Figure from [71]. Right: Reduced binding energy and angular momentum and GW frequency at the moment of merger as a function of the $\xi(\kappa_2^T, \nu)$ parameter (Eq. 10) from the CoRe database of simulations. Note the frequency is the mass rescaled one in dimensionless units, $\hat{f}_{\text{mrg}} = M f_{\text{mrg}}$. Gray bands represent the fit 90% confidence region. Figure adapted from [72].

binary computed as [73, 74]

$$E_b = -\frac{M - \Delta E_{\text{GW}}}{\mu} = \frac{(M_{\text{ADM}} - \Delta \mathcal{E}_{\text{GW}}) - M}{\mu} \quad (8)$$

$$j = \frac{J_{\text{ADM}} - \Delta \mathcal{J}_{\text{GW}}}{M\mu}, \quad (9)$$

where Δ^*_{GW} are the radiated energy and angular momentum computed from the multipoles $h_{\ell m}$, $^*_{\text{ADM}}$ are the Arnowitt-Deser-Misner energy and angular momentum (perpendicular to the orbital plane) at the beginning of the simulation and M is the binary mass. During the evolution the binary emits energy and angular momentum and both j and E_b decrease from their initial values, Fig. 2 (left panel).

As suggested by Fig. 1, the GW quantities (frequency, peak amplitude and luminosity) and thus also the energetics are very dependent on the binary mass, mass ratio as well as on the NS EOS and spins (the latter are not shown in the figure). However, using the analytical estimates presented above it is possible to describe all the numerical data in simple terms. At sufficiently high frequencies the short range tides significantly contribute to the binary interaction energy⁴ and the key quantities of the GW and the energetics at a fix time close to the moment of merger are functions of the tidal parameter [75]. For example, the properties of every simulated equal-mass binary at the moment of merger are very well captured by κ_2^T solely. The fact that the latter

⁴ A more precise and formal argument is discussed in [75, 72].

parameter encodes to a very good accuracy the EOS effect is sometimes referred to as quasiuniversality; relations like $f(\kappa_2^T)$ are called EOS-independent or EOS-insensitive relations. Mass-ratio effects up to $q = M_A/M_B \sim 2$ can be described by further considering the parametrization

$$\xi = \kappa_2^T + \gamma(1 - 4\nu) , \quad (10)$$

where $\nu = \mu M \in [0, 1/4]$ and γ is a fitting parameter [72].

Figure 2 shows the robustness of this description for a large number of irrotational BNS simulations. More compact (small κ_2^T) and more massive binaries emit more energy, as expected. A fiducial equal-mass merger emit about 3-4% of the mass in GW by the end of the chirp phase (irrotational binaries). The angular momentum of the system at merger is larger the less compact is the binary and the larger is the mass ratio q (smaller ν). In other terms, binaries with NS with large radii merge at larger separations. The GW merger frequency can be fit to a simple function,

$$f_{\text{GW}}^{\text{mrg}} \simeq 2.405 \left(\frac{1 + 1.307 \cdot 10^{-3}\xi}{1 + 5.001 \cdot 10^{-3}\xi} \right) \left(\frac{M}{2.8M_\odot} \right) \text{ kHz} , \quad (11)$$

with $\gamma \simeq 3200$. Similar relations exists for all the relevant dynamical quantities, such as the binding energy, the angular momentum, or the GW luminosity at merger [76, 61, 72]. The results above do not include the effects due to the NS rotation. The largest effect in case of spinning merger is due to spin-orbit interactions that depends, in first approximation, on the magnitude and sign of projection of the spin along the orbital angular momentum, S_z . For small spins, for example, the effect is linear in spin and the angular momentum at merger is $j_S \approx j_0 \pm S_z/M\mu$ [77, 76].

We shall see in the following that κ_2^T (or \tilde{A}) is a useful “order parameter” also for some properties of the remnant. While there is no binary dynamics in the latter case, the remnant quantities (at early times) are largely determined by the conditions at merger.

3 Prompt collapse

Prompt BH collapse mergers can be defined as those merger in which the NS cores collision has no bounce (See description in Sec. 5), but instead the remnant immediately collapses at formation. Prompt collapse happens within $\sim 1 - 2$ ms from the moment of merger and can be identified by the maximum density monotonically increasing to the collapse, Fig. 3. This definition of prompt collapse implies negligible shocked dynamical ejecta because the bulk of this mass ejection comes precisely from the (first) core bounce [30] (see Sec. 7.) An example of merger waveform for a prompt collapse is shown in the first panel of Fig. 1.

Numerical-relativity simulations predict that circular and equal-mass BNS merger will be followed by a prompt collapse to a BH, if the total gravitational

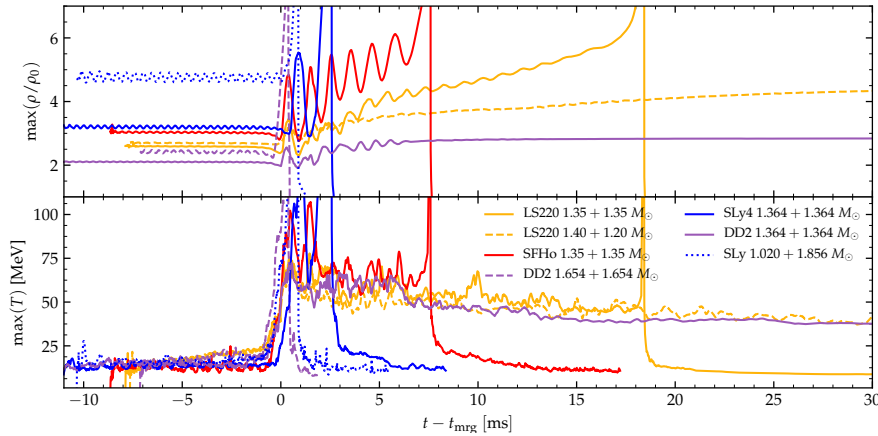


Fig. 3 Evolution of the maximum density and temperature during mergers of representative binaries. The legend indicate the total mass. The DD2 1.654 + 1.654 M_{\odot} is an example of prompt collapse; SLy 1.020 + 1.856 M_{\odot} is an example of accretion induced prompt collapse. In both cases the maximum density monotonically increases to the collapse. SLy 1.364 + 1.364 M_{\odot} , SFHo and LS220 1.35 + 1.35 M_{\odot} are short-lived remnants collapsing to BH at different times. Note the oscillations in the maximum density related to the NS cores bounces and correlated to the temperature peaks. The LS220 1.20 + 1.40 M_{\odot} shows that moderate mass ratios can increase the lifetime of the remnant (compare to the LS220 equal mass case). The DD2 1.364 + 1.364 M_{\odot} is an example of long-lived remnant surviving for more than 100 ms. Figure adapted from [30, 27, 78].

mass M of the binary exceeds a threshold mass, given by [19, 20]

$$M_{\text{pc}} = k_{\text{pc}} M_{\text{max}}^{\text{TOV}}, \quad (12)$$

where k_{pc} depends on the unknown EOS. Current simulations of irrotational, $q \sim 1$ BNS spanning a sample of 18 hadronic EOS and comparable masses find that $1.3 \lesssim k_{\text{pc}} \lesssim 1.7$ [19, 20, 61, 79, 80]. For these data k_{pc} shows an approximately EOS-insensitive linear behaviour in the compactness C (or in the radius) of a reference nonrotating NS at equilibrium [20]. For example, using the extended set of data from [19, 20, 80], and choosing the maximum NS compactness as reference one finds the best fit [81]

$$k_{\text{pc}}(C_{\text{max}}) = -(3.29 \pm 0.23) C_{\text{max}} + (2.392 \pm 0.064). \quad (13)$$

Note that under the hypothesis that the merger did not promptly form a BH, the inversion of Eq. 12 leads to a bound on the maximum NS mass. This argument can be used to estimate the maximum NS mass after GW170817, by interpreting the GW counterpart as evidence for a NS remnant [82, 83, 84, 85].

An alternative model for the prompt collapse threshold based on NR data is based on the tidal parameter κ_2^T [61]. An analysis of comparable-mass data of the CoRe collaboration finds that all the reported prompt collapse mergers

are captured by the condition ⁵

$$\kappa_2^T < \kappa_{\text{pc}}^T \approx 80 \pm 40 . \quad (15)$$

The above is a EOS-insensitive rule of thumb. For equal-mass BNS the κ_2^T can be interpreted as a measure of the binary compactness with more compact binaries leading to earlier BH formation. Note that Eq. 15, differently from Eq. 12 contain a dependence on the mass ratio. Improved phenomenological descriptions of the collapse threshold could be obtained by combining this criterion with the threshold mass criterion above [86].

The above prompt collapse models are valid for comparable masses and irrotational (no NS spin) mergers. For a given total mass, moderate mass ratios can extend the remnant lifetime with respect to equal mass BNS because of the less violent fusion of the NS cores and a partial tidal disruption that distribute angular momentum at larger radii in the remnant [20]. If the total mass is sufficiently large, the primary can be close to $M_{\text{max}}^{\text{TOV}}$ and the material accreting from the (partial) tidal disruption of the companion can favour a prompt collapse. Moreover, spin-orbit interactions have repulsive or attractive character depending on the sign of the spin projection along the orbital angular momentum (spins aligned or antialigned). Hence, they can either increase (or decrease) the angular momentum support of the remnant and delay (anticipate) BH collapse [87, 77, 88].

The prompt collapse models above indeed fail for large mass ratio $q \sim 1.5 - 2$ [78]. In BNS with increasing mass ratio and fixed chirp mass, the companion NS undergoes a progressively more significant tidal disruption. For sufficiently soft EOS, the collapse in these mergers is triggered by the accretion of the companion onto the massive primary star. This “accretion-induced prompt collapse” scenario should be always present after a critical mass ratio in connection to the maximum NS mass. A rough estimate of the threshold is given by modifying Eq. 12 as $M_{\text{pc}}(\nu) \sim M_{\text{pc}} \cdot (4\nu)^{3/5}$, and it indicates that extreme mass ratios favour prompt collapse.

A systematic numerical-relativity investigation of the prompt collapse threshold varying parametrized EOS, masses, mass ratio and spin is presently missing but rather urgent for a quantitative understanding of the merger dynamics. Related to this, it remains challenging to construct a EOS-insensitive (universal) relation for robustly determining the prompt collapse from binary properties.

4 Remnant black holes

Black holes produced by the collapse of irrotational binary merger remnants (either prompt collapse or short-lived) are found with dimensionless spin [89,

⁵ The corresponding value in \tilde{A} is

$$338 \lesssim \tilde{A}_{\text{pc}} \lesssim 386 . \quad (14)$$

87, 77, 71, 90, 78]

$$0.6 \lesssim a_{\text{BH}} \lesssim 0.875 . \quad (16)$$

This interval can be expected from the merger quasiuniversal relations presented in Sec. 2. The relations $E_b^{\text{mrg}}(\kappa_2^{\text{T}})$ and $j_{\text{mrg}}(\kappa_2^{\text{T}})$ at the moment of merger give upper limits for the BH mass and spin

$$M_{\text{BH}} < E_b^{\text{mrg}} \nu M \quad \text{and} \quad a_{\text{BH}} < j_{\text{mrg}} \nu , \quad (17)$$

assuming the remnant would instantaneously collapse to BH without GW emission nor remnant disc/ejecta. The reduced angular momentum interval in Fig. 2 is $3.2 \lesssim j_{\text{mrg}} \lesssim 3.8$, with smaller values obtained for smaller κ_2^{T} . Since binaries with $\kappa_2^{\text{T}} \gtrsim 250$ have stiff EOS and long-lived remnant and short-lived binaries emit in GW at least the same amount of binding energy that possesses at merger (Fig. 1, left panel), one can focus to binaries that prompt collapse $\kappa_2^{\text{T}} < 120$ (Eq. 15) and obtains $a_{\text{BH}} < 0.875$ for equal-mass BNS $\nu = 1/4$.

The largest BH spins, $a_{\text{BH}} \sim 0.8$, are obtained for equal-mass prompt collapse mergers. Note that in the latter case the postmerger GW luminosity is comparable to that of the moment of merger and that very light discs are formed. For large mass ratios the angular momentum at merger is distributed in massive accretion disc and the BH spin are below the upper limit (see Sec. 6). Black holes formed by the collapse of short-lived NS remnant have typically smaller spins than those produced in prompt collapses (for a given mass), because their postmerger GW is very luminous (Sec. 5) and they are surrounded by massive accretion discs (Sec. 6).

Remnant BHs can spin up due to the disc accretion and, in principle, can reach almost maximal spins [91, 92]. In practice however, Keplerian disc in merger remnant are too light to significantly spinup the BH. Moreover, ordered poloidal magnetic fields between the disc and the horizon can transport angular momentum outward into the bulk of the disc and even arrest the accretion [93, 94, 95]. The disc accretion can be further modified by the angular momentum losses due to winds on the same timescales [96, 97, 98]. The launch of a jet might also spindown the BH [99]. The evolution of the remnant BH on timescales of seconds is an open question related to the evolution of the accretion disc (Sec. 6).

The upper limits on the BH rotation inferred from NR simulations should be considered in models of electromagnetic counterparts. For example, in short-gamma-ray burst models (SGRBs) the energy deposition by neutrino pair-annihilation depends strongly on the BH spin [100]. For fixed accretion rate, the energy deposition by neutrinos from a disk accreting onto a BH with $a_{\text{BH}} = 0.7$ can be up to a factor 100 times smaller than for a disk feeding a maximally spinning BH. On the other hand, a_{BH} does not significantly constrain SGRB models invoking magnetic mechanisms, which can easily account for the required energies even in absence of extremely high BH spin [101]. Note that in the Penrose/Blandford-Znajek mechanism the BH rotational energy is extracted at a rate proportional to a_{BH}^2 at leading order in spin [102, 95].

5 Remnant neutron stars

The observations of pulsars with masses $\sim 2M_\odot$ [103, 104] constrains EOS models to support maximum masses larger than those observed. In this case, a most likely outcome of a fiducial $M \sim 2.8M_\odot$ merger is a NS remnant, e.g. [19]. The properties and evolution of these NS remnant discussed here below are subject of intense research and closely linked to kiloHertz GW and mergers' counterparts.

It is customary to define short-lived NS remnants those that collapse on dynamical timescales of several rotational periods (tens of milliseconds), and long-lived remnants those collapsing on significantly longer timescales. Often, short-lived remnant are indicated as hypermassive NS (HMNS) and long-lived remnants are indicated supramassive NS (SMNS) and massive NS (MNS) if the remnant rest-mass is below the nonrotating equilibrium limit, $M_{\text{max}}^{\text{TOV}}$. Throughout this work we do not use the names HMNS and SMNS for merger remnants⁶ since these names refer to general-relativistic zero-temperature axisymmetric equilibrium configuration, but mergers remnants are not cold equilibria. In particular, a HMNS is defined as a differentially rotating NS at equilibrium with mass above the rigidly rotating limit [105], while a SMNS is a rigidly rotating NS at equilibrium with rest mass exceeding the nonrotating limit $M_{\text{max}}^{\text{TOV}}$ [106, 107].

The evolution of the remnant can be approximately separated in an early (dynamical) GW-driven phase and a secular phase that is (initially) driven by viscous magnetohydrodynamical process and neutrino cooling. The fate of the remnant is determined by a complex interplay of gravitational, nuclear, weak and electromagnetic interactions that often act on comparable timescales.

Dynamical (GW-driven) phase. At formation, NS remnants are very dynamical. The maximum density and temperature increase immediately after merger as a consequence of matter compression and the NS cores bounce several times, e.g. [27]. The more massive the binary and the more compact the binary is the faster and the more violent the dynamics is. Despite the large relative collision speed, the speed of sound at densities $\rho \gtrsim \rho_0$ is $c_s \gtrsim 0.2c$ and prevents the formation of hydrodynamical shocks inside the cores. Only at the surface of the NSs pressure waves can steepen into shock waves which accelerate matter at the edge of the remnant up to mildly-relativistic speeds (Sec. 7). Thus, matter inside the cores remains cold ($T \lesssim 10 \text{ MeV}$) and, while the densest part of the cores rotate and fuse, the compressed matter at the contact interface is pushed outwards. Matter moving outwards reaches temperature up to $T \sim 70\text{--}110 \text{ MeV}$ and forms a pair of co-rotating hot spots displaced by an angle of $\sim \pi/2$ with respect to the densest cores, e.g. [108]. The bound matter expelled from the center forms a disc which is fed by the central remnant with hot and outgoing density spiral waves streamig from the central region (Sec. 6.)

⁶ Note, however, the nomenclature is retained in some of the presented figures.

The large temperatures in the remnant determine large neutrinos production and an early burst in neutrino luminosity reaching $\sim 10^{52-53}$ erg/s, e.g. [109, 26, 110, 111]. Simulations including neutrino transport predict the mean neutrino energies at infinity $E_{\nu_e} (\sim 10 \text{ MeV}) \lesssim E_{\bar{\nu}_e} (\sim 15 \text{ MeV}) \lesssim E_{\nu_{\mu,\tau}} (\sim 20 \text{ MeV})$, with more massive binaries and softer EOS resulting in higher mean energies [26, 112, 113]. Due to the strong dependence of the cross-sections on the incoming neutrino energy, neutrinos with different energies decouple from matter from very different regions. While average energy ν_e and $\bar{\nu}_e$ decouple at densities between a few and several times $10^{11} \text{ g cm}^{-3}$, respectively; low energy neutrinos decouple at around $10^{13} \text{ g cm}^{-3}$ along spheroidal neutrino decoupling surfaces [114, 113]. Because free neutrons are abundant, the absorption opacities for ν_e are larger than those for $\bar{\nu}_e$, while pair processes, responsible for keeping $\nu_{\mu,\tau}$ and their antiparticle in equilibrium, decouple at much larger densities and temperatures inside the remnant. Electron neutrino and positron absorption on neutrons increases substantially the electron fraction in the material, with a larger effects in hotter remnant and along the polar regions, where neutrino fluxes are more intense due to the lower optical depths [45, 115, 116, 117, 118, 119].

New degrees of freedom or new matter phases in the EOS at extreme densities $\sim 3-5\rho_0$ can also impact the remnant dynamics and leave detectable imprints on the GW. Examples are matter models including hyperon production [120, 121] or zero-temperature models of phase transitions to quark-deconfined matter [122, 123]. In both cases, the EOS models soften at extreme densities thus favouring more compact remnants and their gravitational collapse. Their impact on the dynamics crucially depends on the densities at which the EOS softening (or stiffening) takes place. Postmerger GWs at kiloHertz frequencies carry, in principle, the signature of the EOS change, that could be observed for transition happening at sufficiently low densities. However, the unambiguous extraction of information from these detections will be heavily model dependent [72].

The dynamical phase described above lasts for about $\sim 10-20$ milliseconds until the cores have completed their fusion or collapsed to BH. During the core fusion, the remnant is a strongly deformed object with a pronounced bar-like deformation that powers a significant emission of GWs. The main postmerger GW signature is a short transient with a spectrum peaking at a few characteristic frequencies. The dominant peak frequency is associated with twice the rotation frequency of the remnant NS at frequency f_2 [16, 21, 22, 124, 23, 24, 25, 125, 126, 90, 88]. These GW frequencies can be robustly computed from short and nonexpensive simulations, thus have been studied in great detail. We refer to the literature above for detailed analysis and their association to the hydrodynamical modes in the remnant.

The postmerger peak frequencies approximately correlate to the properties of the binary and to properties of the nonrotating NS equilibria constructed with the same EOS [22, 23, 127, 24, 25, 128, 129, 130]. EOS-insensitive phenomenological descriptions of the postmerger GW's main features are thus possible. As an example, Fig. 4, shows a representation of the peak post-

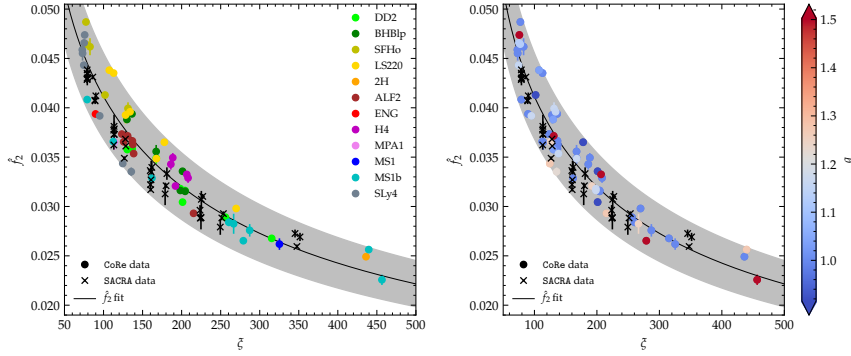


Fig. 4 Phenomenological EOS-insensitive relation between the GW’s main peak postmerger frequency and the (modified) tidal parameter $\xi(\kappa_2^T, \nu)$ (Eq. 10). Both panels show the same data. The round markers correspond to the simulations of the **CoRe** database. For those data the EOS variation is highlighted in colors in the left panel and the mass ratio variation in the right panel. The crosses correspond to the **SACRA** database that also refer to a large variation of EOS (although not highlighted in the graphics). Note the frequency is the mass rescaled one in dimensionless units, $\hat{f}_2 = Mf_2$. The fit is performed only on the **CoRe** data and the gray band represents the 90% confidence region. Figure adapted from [72].

merger frequency in terms of κ_2^T [25]. The basic idea behind this fitting model is that the angular momentum available at merger determines the rotational frequency of the bulk mass, and that the GW is efficiently radiated in short time at this frequency. Note, however, that the postmerger waveform is not formed by a set of discrete frequencies but rather the frequency evolves continuously in a nontrivial way, increasing -on average- in time as the remnant become more compact. EOS-insensitive relations are the base to construct simple analytical representation of the postmerger GW [23, 131, 132, 133, 72]. Application of these models to constrain on matter at extreme densities inferred from the kiloHertz GW are discussed in various works, e.g. [127, 134, 135, 72].

The GW luminosity depends strongly on the merger remnant, Fig. 1. For prompt collapse mergers the GW luminosity peaks are the largest and happen shortly after the moment of merger. Short-lived remnants have multiple peaks of comparable luminosity on a time scale of few milliseconds and corresponding to the bounces of the NS cores. Long-lived (and stable) NS remnants are qualitatively similar to the short-lived but the the luminosity is less intense due to the smaller compactness.

A main difference with respect to binary black holes is that the most luminous mergers do not correspond, in general, to those that radiate the largest amount of energy. The largest GW energies per unit mass are radiated by short-lived remnant over typical timescales of few tens of milliseconds after the moment of merger [71]. This is because a bar-deformed remnant NS close to gravitational collapse is a very efficient emitter of GWs. The analysis of the energetics from the simulations indicates that about two times the energy

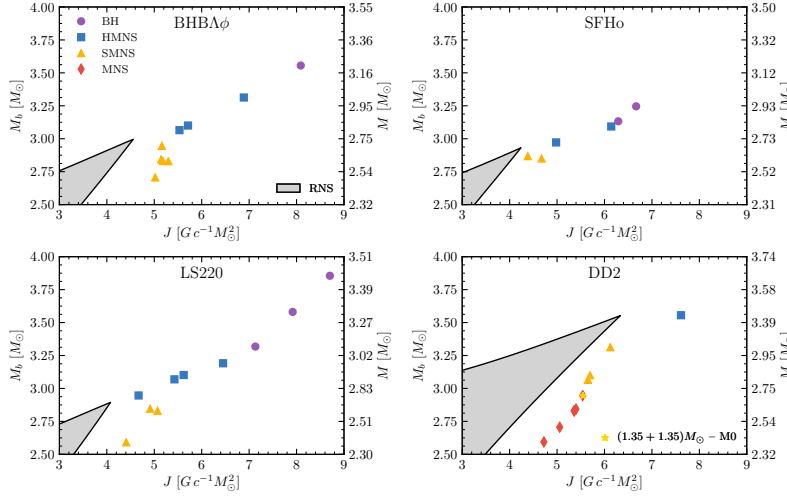


Fig. 5 Diagrams of the rest-mass vs. angular momentum for representative merger remnants after the GW-dominated phase. The markers indicate remnants from fiducial mergers $M \sim 2.7 - 2.8 M_\odot$, $q \sim 1$ and microphysical EOS. The gray region is the stability region of rigidly rotating equilibria constructed assuming zero temperature and neutrino-less beta equilibrium [136]. For a fixed J lower and upper boundaries of the shaded areas are set by the mass shedding and maximum mass limit, respectively. The tip of the shaded region marks the maximum baryonic mass configuration supported by each EOS in the case of rigid rotation. Figures from [28].

emitted during the inspiral and merger can be emitted during the postmerger phase, Fig. 2. While the merger energy and peak luminosity tightly correlates with κ_2^T , the GW emitted by the remnant (and thus the total energy) has a more complex behaviour [61]. An absolute upper limit to the GW energy estimated by about one hundred simulations of the CoRe collaboration is

$$E_{\text{GW}} \lesssim 0.126 \left(\frac{M}{2.8 M_\odot} \right) M_\odot c^2. \quad (18)$$

Secular (Viscosity-driven) phase. As the GW emission of energy and angular momentum backreacts on the fluid, it quickly damps nonaxisymmetric modes in the remnant that evolves towards axisymmetry. The GW-emission timescale estimated at the end of the dynamical phase is [28]

$$\tau_{\text{GW}} = \frac{J}{\dot{J}_{\text{GW}}} \gtrsim 0.5 \text{ s}. \quad (19)$$

At this point the dynamics becomes dominated by viscous and cooling processes.

The NS remnants that did not collapse to BH have angular momenta significantly exceeding the mass-shedding limit for rigidly rotating NS [28]. Figure 5 shows a diagram of the baryon mass and the angular momentum

of the remnant for a sample of mergers, and it compares them to the rigidly rotating zero-temperature and beta-equilibrated isolated NS equilibria (gray shaded region). The GW-driven phase in mergers’ remnants always ends on the right of the shaded areas; these remnants could be called “super-Keplerian”. Moreover, long-lived remnants have gravitational masses $\sim 0.08 M_\odot$ larger than the corresponding equilibrium models having the same baryonic mass, but zero temperature [28]. A key open questions for future simulations is the evolution of these systems on timescales of hundreds milliseconds to seconds postmerger.

The basic properties that determine the evolution are the remnant rotation and its temperature and their evolution under magnetohydrodynamical processes and neutrino cooling and heating. On the one hand, finite temperature and finite neutrino chemical potential contribute to $\sim 10\%$ increase of the pressure in the NS core [137, 27]. But this is not sufficient to significantly alter the maximum nonrotating mass due to the degeneracy of matter above ρ_0 . On the other hand, thermal support inflates the regions with subnuclear densities increasing the NS radius. For characteristic temperatures, the radius of a fiducial NS $R_{1.4}$ increases of about $20 - 40\%$ (depending on the EOS) comparing to the zero-temperature nonrotating case.

Rotational support also increases the maximum NS mass. For example, in the limiting case of rigid rotation at the Keplerian limit, the maximum NS mass is increased by $\sim 20\%$ with respect nonrotating NS. Since this affects the whole star, the NS radius is typically increased by $\sim 40\%$, but at the same time the central density is decreased by a similar amount, if one compares nonrotating and Keplerian NSs of identical masses. Interestingly, at temperatures reached in merger remnant, the maximum mass for a stable rigidly-rotating “hot” NS remnant is actually smaller than that for cold equilibria [137]. Rigidly-rotating NS with temperature profiles similar to those found in simulations can support $\sim 0.1 M_\odot$ less baryonic mass than cold configurations. While it is unlikely that finite temperature and composition effects can stabilize a merger remnant against gravitational collapse, larger radii imply that the mass shedding limit is reached at lower angular frequencies. Hence, a NS remnant classified SMNS according to the cold EOS could actually be a HMNS. Alternatively, it is possible to form SMNS remnants with baryonic masses and thermodynamical profiles for which there is no rigidly-rotating equilibrium.

Magnetic fields also introduce additional pressure and can increase the maximum mass and the maximum velocity of rigidly rotating isolated NS. However, the changes in maximum mass are moderate and up to $15 - 30\%$ for extreme values of the magnetic field $B \sim 10^{18}$ G [138]. In merger remnants, magnetohydrodynamics instabilities and magnetic-field amplifications can lead to global-scale magnetic effects and angular momentum redistribution in the remnant [139, 140, 141, 142, 32, 143]. These instabilities operate on length scales of meters to centimeters, and it is presently impossible to perform fully-resolved, global merger simulations with realistic initial conditions. High-resolution simulations of merger with magnetar-strengths magnetic fields showed that the Kelvin-Helmholtz instability at merger could amplify the magnetic-field energy to up to 1% of the thermal energy [144]. Moreover, if tur-

bulent stresses are modeled by an effective α -viscosity, these simulations estimate $\alpha \simeq 0.01\text{--}0.02$ at $\rho \lesssim 10^{13} \text{ g cm}^{-3}$ (disc's densities) and $\alpha \sim 10^{-4}\text{--}10^{-3}$ at higher densities [142]. Assuming the α -viscosity model [145], the angular momentum redistribution in the remnant happens on a timescale [23]:

$$\tau_{\text{visc}} \simeq \alpha^{-1} R_{\text{rem}}^2 \Omega_{\text{rem}} c_s^{-2} \simeq 0.56 \text{ s} \left(\frac{\alpha}{0.001} \right)^{-1} \left(\frac{R_{\text{rem}}}{15 \text{ km}} \right)^2 \left(\frac{\Omega_{\text{rem}}}{10^4 \text{ kHz}} \right) \left(\frac{c_s}{0.2c} \right)^{-2}, \quad (20)$$

where Ω_{rem} and c_s are the remnant angular velocity and typical sound speed, respectively. Simulations including a physically motivated prescription for viscosity in GR find that the remnant becomes more quickly axisymmetric, possibly reducing the postmerger GW emission [146, 147]. In particular, the turbulence induced by the magnetic field favours angular momentum redistribution and accelerate the collapse [23, 146].

The rotational profiles of NS merger remnants have a minimum at their center [34, 148, 149, 108, 150, 151], so the remnant's core is expected to spin up during its evolution [146]. Consequently, it is unlikely that the angular momentum remnants is redistributed so to trigger gravitational instability of the core. This indicates that a super-Keplerian remnant evolving towards equilibrium must shed excess angular momentum. Because the angular momentum losses cannot be GW-driven (Eq. 19) they must be driven by viscous effects on timescales of τ_{visc} . Angular momentum can be also removed by other electromagnetic processes that can extract the rotational energy of the remnant, e.g. [152, 153]. These processes can very efficiently generate large outflows because the mass shedding limit moves to lower J with decreasing M_b [29, 30]. Simulating timescales τ_{visc} is challenging for ab-initio numerical simulations. Such a regime is currently explored in simplified setup (Newtonian gravity, axisymmetry, ad-hoc initial conditions, etc. Sec. 6). Together with viscous processes, neutrinos interactions are the other key process for the remnant evolution. The main effect is cooling, that operate on timescales up to $\tau_{\text{cool}} \sim 2\text{--}3 \text{ s}$ [44, 109, 154, 26]. The excess of gravitational binding energy in the remnant is likely radiated in the form of neutrinos. These conditions are analogous to those found in newly born NS in core-collapse supernovae (e.g. [155, 156, 157, 158, 159]).

A possible outcome of the viscous evolution of a long-lived remnants is a rotating NS close to the mass shedding limit with spin periods $P_0 \lesssim 1 \text{ ms}$. Comparing possible evolution scenarios to equilibrium sequences, it is possible to estimate [28]

$$P_0 = \left[a \left(\frac{M_b}{1 M_\odot} - 2.5 \right) + b \right] \text{ ms}, \quad (21)$$

with EOS-dependent coefficients $a \sim -(0.2\text{--}0.3)$ and $b \sim 1$. Note that the above estimate gives spin periods significantly smaller than those typically inferred for the progenitors of SGRB with extended emission in the context of the magnetar model, $P_0 \sim 10 \text{ ms}$ [160, 161]. Gravitational-wave losses could however continue past the viscously-driven phase of the evolution and further spin down the remnant over a timescale of many seconds to minutes [160,

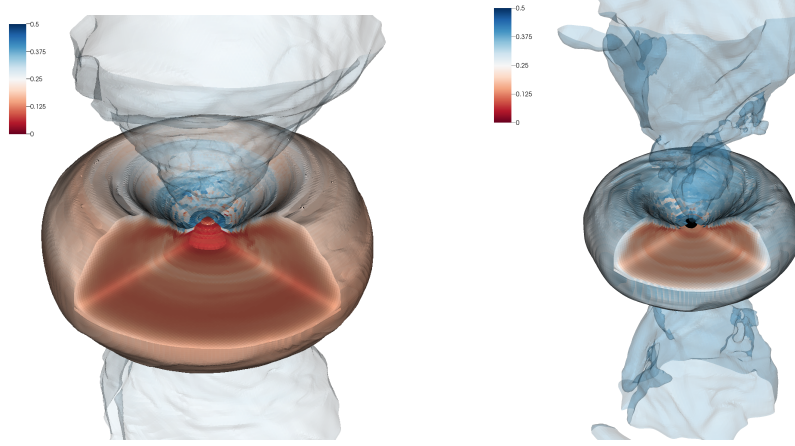


Fig. 6 Example of discs around NS (left) or BH (right) remnants. The figure shows a 3D rendering of the electron fraction for equal-masses BNS described by the DD2 (left) and SFHo (EOS). Both images have the same spatial scale and show the data in a box of size 750 km. The electron fraction is used to color the 10^7 gcc (semi-transparent) and the 10^{11} gcc density isosurfaces. The 10^{13} gcc isosurface is also shown for the DD2 model. The black surface in the SFHo model denotes the approximate location of the black hole horizon. The accretion discs are fairly neutron rich in their bulk, irrespective of the remnant type (massive NS or black hole). The accretion disk coronae are irradiated by neutrinos and are less neutron rich. Figure from [27].

162]. This GW emission could be driven by secular instabilities in the remnant [163, 164, 8, 9, 165, 10, 11, 12, 166, 167, 125, 128, 168], or by deformations due to a strong toroidal field [160]. For example, the GW luminosity of the one-armed instability during the first ~ 50 ms of the post-merger evolution is $\sim 10^{51} \text{ erg s}^{-1}$ and does not show strong evidence for decay [167, 125]. If the one-armed instability were to persist without damping, then it would remove all of the NS remnant rotational energy, which is $\sim 10^{53} \text{ erg}$ [82], over a timescale of ~ 100 s. This timescale is compatible with the spin-down timescale inferred from the magnetar model [160]. This GW signal from the one-armed instability could be detectable by LIGO-Virgo up to a distance of ~ 100 Mpc for optimally oriented sources [125].

6 Remnant discs

Following a common convention, the remnant disc is here defined as the baryon material either outside the BH's apparent horizon or the one with densities $\rho \lesssim 10^{13} \text{ g cm}^{-3}$ around a NS remnant. The baryonic mass of the disc is computed in simulations as volume integrals of the conserved rest-mass density and it is referred to as M_{disc} . Remnant discs are thick accretion disc with typical aspect ratio $H/R \sim 1/3$ and mass between $0.001\text{--}0.2 M_{\odot}$. The structure and composition of the remnant discs can significantly depend on the different formation mechanisms due to the binary properties.

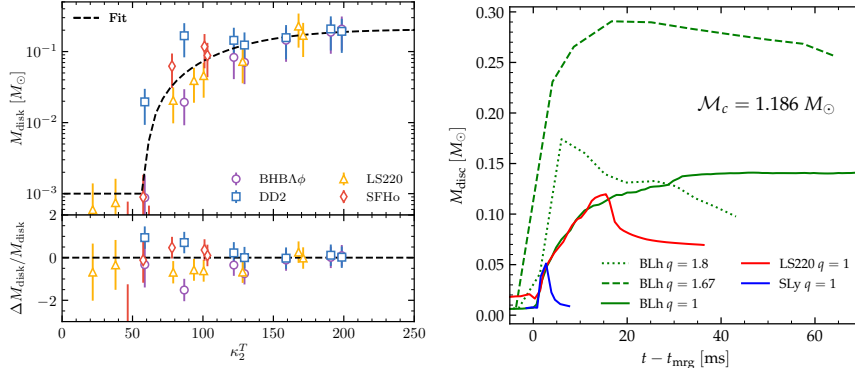


Fig. 7 Disc masses as a function of the tidal parameter and disc mass evolution for representative case. Left: The remnant disc mass of equal-mass mergers correlate with κ_2^T , the latter measuring the binary compactness. Small values $\kappa_2^T \lesssim \kappa_{pc}^T$ correspond to prompt collapse merger for which a negligible disc form. Figure from [30]. Right: Disc formation and early evolution for mergers with chirp mass $1.186 M_\odot$. The $q = 1$ SLy and LS220 are short-lived remnants collapsing to BH within 2 and 18 milliseconds respectively. The BLh $q = 1, 1.67$ are long-lived remnants, while the $q = 1.8$ is an accretion induced prompt collapse. Figure adapted from [78].

In the case of comparable mass mergers, the accretion disc is formed during and after the merger by the matter expelled by tidal torques and by the collision interface. Because of the different temperatures in the tidal tail (cold) and collisional interface (hot), the disc is initially highly non-uniform. As time evolves, the NS remnant continuously sheds mass and angular momentum into the disc with spiral density waves (Sec. 5), thus increasing the mass of the disc and generating mass outflows [71, 28] (Sec. 7). The continue action of shocks and spiral waves increases the entropy in the disc and eventually produces an approximately axisymmetric Keplerian disc characterized by a temperature profile that changes smoothly from ~ 10 MeV (for $\rho \simeq 10^{13}$ gcc) down to ~ 0.1 MeV (for $\rho \simeq 10^4$ gcc). The electron fraction is reset by pair processes and the entropy per baryon varies between 3 and several 10's of k_B/baryon [27]. In general, BH formation significantly affects the disc properties, Fig. 6. If the central object collapses to a BH, approximately half of the disk mass is swallowed inside the apparent horizon within a dynamical timescale, and the maximum density decreases to a few times 10^{12} gcc. Discs around a BH remnant are in general more compact and achieve higher temperatures and entropies ($\Delta s \simeq 2 k_B/\text{baryon}$) than discs hosting a NS remnant.

Disc masses at formation are shown in the left panel of Fig. 7 as a function of the tidal parameter κ_2^T . Again, the choice of κ_2^T for this plot is to correlate the disc with a measure of the binary compactness [Note however that the

parameter is not a good choice for cases dominated by tidal disruption⁷. The figure highlights that for $q \sim 1$ prompt collapse mergers do not form massive discs (Cf. Eq. 15), because the mechanism primarily responsible for the formation of the disc shuts off immediately in these cases, e.g. [34, 35, 37]. Short-lived and long-lived remnants have instead discs with initial masses $\sim 0.2 M_\odot$. Mergers of BNS with mass ratios up to $q \sim 1.3 - 1.4$ produce more massive discs than $q = 1$ because of the larger centrifugal support and a partial tidal disruption of the companion NS [33, 34, 35, 36, 90].

In high mass-ratio mergers $q \gtrsim 1.5$ the companion NS is tidally disrupted and the disc is mainly formed by the tidal tail [78]. The latter is launched prior to merger and massive accretion discs are possible even if prompt BH formation occurs [31, 78]. The angular momentum of these discs can be $\sim 60\%$ larger than that of discs around BH resulting from the prompt collapse of equal-mass mergers. Moreover, due to the absence of strong compression and shockes, the discs formed in high mass-ratio mergers are initially colder and more neutron rich than those of comparable-mass merger having the same chirp mass.

Examples of disc mass evolutions at early times from formation for different remnants are shown in the right panel of Fig. 7. The figure clearly shows the rapid accretion in case of equal-masses ($q \sim 1$) mergers and BH formation. Discs around NS remnants instead can also increase their mass over time as the remnant's spiral waves propagate outwards. The accretion of discs around BH formed in high-mass-ratio mergers is instead slower due to the larger extension and angular momentum. Here, however, accretion is further driven by the fallback of the tidal tail that perturbs the disc inwards [78].

The long-term evolution of these discs is key for electromagnetic emission. Studies in this direction are becoming more complete and detailed [38, 39, 40, 58, 42, 41, 29, 171, 60, 172], but the challenges related to the simulation of multiple scales and multiple physics have so far required to adopt some simplifications. All of the published simulations adopted somewhat artificial initial conditions (not derived from merger simulations), or neglected important physical effects such as neutrino emission and absorption, or assumed axisymmetry, or did not follow the evolution for sufficiently long times. Crucial questions are related to the development of ordered large-scale magnetic fields formed by dynamo processes and the interplay with neutrino interactions. Large-scale magnetic fields can power relativistic jets [173, 174, 175] and drive mildly relativistic outflows [41, 176, 60]. Neutrino emitted from the hottest and densest part of the remnant irradiate the low density part of the disk (and the expanding wind) thus increasing substantially the electron fraction in the material [171]. The larger effects are for hotter remnant and along the polar regions, where neutrino fluxes are more intense due to the lower optical depths [45, 114, 115, 116, 117, 171, 118, 119, 113].

⁷ An extreme case is for the example the disc mass in black-hole–neutron star binaries, that does not show strong correlation with κ_2^T , [169, 170]. See discussion in [72].

7 Mass ejecta

Since the ejection of neutron rich material happens at different stages of the merger dynamics, mass ejecta have multiple components with different properties, geometries and composition [177, 178].

Dynamical ejecta. Dynamical mass ejecta are generated on a dynamical timescale during the merger process. A fraction of the material is launched by tidal torques close to the moment of merger [54, 116, 90]. Another fraction of matter is unbind from shocks generated after the moment of merger when the cores' bounce [55, 56, 117, 30]. General-relativistic merger simulations indicate the mass of the dynamical ejecta ranges from $10^{-4} M_{\odot}$ to $10^{-2} M_{\odot}$ and that it has characteristic velocities of $0.1-0.3c$ [55, 56, 117, 30]. The tidal ejecta is neutron rich $Y_e \sim 0.1$ and cold, while the shocked ejecta is reprocessed to higher Y_e by pair processes and neutrino irradiation from the NS remnant. The electron fraction in shocked ejecta can span a wide range of values, $Y_e \sim 0.1-0.4$, with the largest Y_e obtained at high latitudes.

For comparable-mass mergers, NR simulations indicate that the shocked component is typically a factor ten more massive than the tidal component. A sample of about 130 simulations using microphysics EOS and approximate neutrino transport indicate that ejecta masses do not strongly correlate in a simple way the properties of the binary [30]. The average mass is $\sim 2 \times 10^{-3} M_{\odot}$ [30]. The mass-averaged electron fraction is $\langle Y_{\text{dyn}} \rangle \sim 0.18$; neutrino absorption has a significant effect on the composition of dynamical ejecta, and some scheme that includes heating must be considered for a realistic estimate of Y_e [45, 179]. Similarly, the ejecta mass-averaged speed is about $\langle v_{\text{dyn}} \rangle \sim 0.18c$, although some part of the ejecta can reach high-speeds up to $\sim 0.8c$ [56, 30]. Dynamical ejecta properties vary with the polar angle and the mass distribution has a rms of $\sim 35^\circ$ [179]. Within the accuracy of the computations, a best model fitting the various simulations is their average. The simulations of the CoRe database for $q < 1.67$ give [30, 179, 180, 113]

$$\overline{m_{\text{dyn}}} = 0.002 \pm 0.004 M_{\odot} \quad (22)$$

$$\overline{\langle v_{\text{dyn}} \rangle} = 0.18 \pm 0.07 c \quad (23)$$

$$\overline{\langle Y_{\text{dyn}} \rangle} = 0.18 \pm 0.10 . \quad (24)$$

where the errorbars contain 90% of the data. These values are compatible within a factor two with those obtained by other groups with independent codes [181, 110, 126, 83, 182, 183]. Numerical errors can account for the difference in some cases, but for the highest resolutions simulated so far they are around 20-40% [83, 30, 78]. Simulations with polytropic EOS or without neutrino leakage, e.g. [55, 56], give ejecta mass and velocities in the same ballpark of those obtained with simulations with microphysics and, at least, a leakage scheme. A compilation of data is presented in [184], although there is a significant statistical and systematical disagreement between those fits and the more recent data. If large-scale magnetic fields are present at the moment of merger,

they could additionally boost the dynamical (shocked) ejecta with a viscous component [185].

For highly asymmetric BNS with $q \gtrsim 1.67$ the dynamical ejecta is instead dominated by the tidal component [181, 126, 78]. The ejecta is distributed more narrowly about the orbital plane and over a fraction of the azimuthal angle around its ejection angle with a crescent shape. Extreme mass asymmetry can boost the mass ejecta by up to a factor four with respect to the equal mass cases (for a fixed chirp mass). In this case, the average electron fraction reduces to ~ 0.11 , and the rms of the polar angle is $\sim 5 - 15^\circ$. This is similar to what observed in black-hole–neutron-star binaries, [186]. The ejecta mass average for equal-mass reported above grows to $\sim 3.3 \times 10^{-3} M_\odot$ if simulations of highly asymmetric binaries are included [78].

In mergers with initially rotating NSs, the dynamical ejecta mass from highly asymmetric mergers with spin aligned to the orbital angular momentum can increase due to the larger angular momentum of fluid elements in the tidal tail [88]. However, for equal-mass mergers the ejecta mass can decrease for large aligned spins [88, 187] because at the moment of merger the system is more bounded (smaller j_{mrg} and more negative E_b^{mrg} as aligned-spin-orbit interaction is repulsive) and less material is unbind from the core shock. Overall, spin effects are sub-dominant with respect to mass ratio effects [88].

Secular ejecta. Another type of ejecta are the secular ejecta originating as winds from the remnant [57, 188, 38, 39, 40, 114, 58, 59, 42, 60, 30]. Long-term Newtonian simulations of neutrino-cooled accretion disks indicate that 10–40% of the remnant disk can be unbound over a timescale of a few seconds. Since remnant discs in mergers have masses up to $\sim 0.2 M_\odot$, secular ejecta are likely to constitute the bulk of the ejecta (if present). These secular ejecta can originate from different physical mechanisms.

Neutrinos from the remnant and the disc drive a wind of material with $Y_e \sim 0.3$ and can unbinding $\lesssim 10^{-3} M_\odot$ [188, 40, 114, 172]. The neutrino wind originates on the disc edge, close to the neutrinosphere, and above the remnant where baryon pollution is minimal. Note that a precise prediction of properties of polar ejecta is presently beyond the possibilities of neutrinos schemes employed in ab-initio NR simulations [40, 42, 189, 172].

Long-term NR simulations have shown that, if the merger outcome is a NS remnant, the spiral density waves propagating from the remnant into the disc can trigger massive and fast mass ejecta [180]. These ejecta start after the moment of merger and operate on timescale longer than the dynamical ejecta. Their origin is purely hydrodynamical but viscosity influences the angular momentum transported by the spiral waves as neutrino transport influences their composition. The spiral wind can have a mass up to $\sim 10^{-2} M_\odot$ and velocities $\lesssim 0.2 c$. The ejected material has electron fraction mostly distributed above $Y_e \sim 0.25$ being partially reprocessed by hydrodynamic shocks in the expanding arms.

Angular momentum transport due to viscous processes causes the disc to spread outwards. Once the accretion rate drops below a critical threshold, neu-

trino cooling becomes ineffective and the disc thermally expands [190, 57, 38]. At this point, nuclear recombination of nucleons into alpha particles provide sufficient energy to unbind $\sim 10\text{--}20\%$ of the disc. The nuclear binding energy liberated in the process is $\simeq 8.8$ MeV/nucleon. Because the disc material starts to recombine where the nuclear energy equals the gravitational binding energy, a characteristic cylindrical radius ϖ^* at which the wind starts is [38],

$$\frac{GM_{\text{disc}}m_b}{\varpi^*} \simeq 8.8 \text{ MeV} , \quad (25)$$

where m_b is the baryon mass. These disc ejecta can be massive and are launched around the equatorial (orbital) plane with characteristic velocities ~ 0.1 c [38, 58, 191]. Magnetohydrodynamics effects can enhance the secular masses and asymptotic velocities and boost the disc ejection fraction to up to $\sim 40\%$ [59, 60]. For long-lived remnants, the composition of the secular ejecta depend sensitively on the lifetime of the remnant due to neutrino irradiation [58, 30].

From the above discussion it should be clear that several properties of the ejecta and thus of the kilonova depend sensitively on the remnant, although these dependencies are not fully quantified yet. This is further indicated by the fact that some of the broad features of synthetic kilonova models applied to fiducial NR data show a correlation with the tidal parameter $\tilde{\Lambda}$ (and hence the merger outcome) [30].

We finally mention the key elements connecting the ejecta and the kilonova emission. For a complete discussion see [53, 178]. The key quantity determining r-process nucleosynthesis in the ejecta is the electron fraction Y_e [192, 178]. If $Y_e \lesssim 0.2$, then the ejecta produces second and third r-process peak elements with relative abundances close to Solar ones. If $Y_e \gtrsim 0.3$, then the material is not sufficiently neutron rich to produce lanthanides but first r-process peak elements are produced. A sharp transition between these two regimes is marked by $Y_e \simeq 0.25$. The Y_e also determines the photon opacity in the material [52, 51], drastically altering the timescale and the effective blackbody temperature of the kN emission [53]. High- Y_e ejecta power kilonovae peaking in the UV/optical bands within a few hours of the merger (blue), while low- Y_e ejecta power kilonovae peaking in the infrared over a timescale of several days (red).

8 Conclusion

It is useful to summarize by focusing on the concrete examples of the two BNS events observed so far, GW170817 [1, 2, 3, 193] and GW190425 [14].

The source of GW170817 has mass $M \simeq 2.73 - 2.77 M_\odot$ and mass ratio up to $q = 1.37$ (1.89) depending on the low (high) spin prior utilized in the GW analysis [1, 2, 3]. The merger was not observed but the merger frequency can be accurately predicted from the probability distribution of $\tilde{\Lambda}$ using the NR fits discussed in Sec. 2. One finds that the (broad) distribution of $\tilde{\Lambda}$ translates

into $f_{\text{mrg}} = 1719_{-214}^{+163}$ Hz [72]. Combining the GW170817 data with the prompt collapse models of Sec. 3, it is possible to rigorously predict via a Bayesian analysis that the probability of prompt BH formation is $\sim 50 - 70\%$. However, if the constraint on the maximum mass $M > 1.97M_{\odot}$ from pulsar observations is imposed, the probability significantly decreases below 10%. Hence, prompt collapse in GW170817 is largely disfavoured [81].

A NS remnant would have emitted GW at the characteristic frequency $f_2 = 2932_{-409}^{+337}$ Hz, that can be again estimated from the \dot{A} posteriors together with the peak GW luminosity [61, 72]. A sufficiently sensitive network of GW antennas could have detected the postmerger GW at f_2 with a peak luminosity larger than 10^{55} erg/s. These frequencies and luminosities might be accessible by improving the design sensitivity of current ground-based GW detectors of a factor two-to-three or with next-generation detectors [194, 135, 195].

The NR-based GW analysis of the prompt collapse supports the mainstream interpretation of the electromagnetic counterparts that suggests the formation of a short-lived NS remnant [82, 196, 83, 37, 85, 84]. AT2017gfo, the kilonova counterpart of GW170817, has both a blue and a red component, thus suggesting that the ejecta had a broad range of compositions with at least a fraction being free of lanthanides. A fit of AT2017gfo light curves to a semi-analytical two-components spherical kilonova model indicates the lanthanide poor (rich) blue (red) component has mass $2.5 \times 10^{-2} M_{\odot}$ ($5.0 \times 10^{-2} M_{\odot}$) and velocity 0.27c (0.15c) [197, 198]. Similar results are obtained using more sophisticated 1D simulations of radiation transport along spherical shells of mass ejecta [199, 200]. The estimated masses are larger than those predicted from NR for the dynamical ejecta and the estimated velocities for the blue component are smaller than those expected for disc winds [191]. Kilonova models with multiple components help resolving the tension [179] because the faster dynamical ejecta can be irradiated by the underlining disc, thus sustain the emission [39, 201, 202]. Also, spiral winds [180] and/or highly magnetized winds [176, 60, 175] contribute in filling the gap.

Within this picture, prompt collapse can be tentatively excluded by the observation of the blue kilonova, in agreement with the GW analysis of [81]. Under the assumption of an equal-mass merger, only a small quantity of shock-heated or disk wind ejecta would be present in this case and it would be inconsistent with the $\sim 10^{-2} M_{\odot}$ inferred from the data [82]. A long-lived remnant could be excluded based on the estimated kinetic energy of the observed kilonova and SGRB afterglow, that are too low for the energy reservoir of a NS remnant at the mass shedding limit. Note alternative scenarios based on the interaction between a relativistic jet and the ejecta exist [203, 204, 205], but they might be disfavoured due to insufficient deposition of thermal energy in the ejecta [206].

Under the assumption that the merger remnant was a short-lived NS, NR models described in Sec. 3 and basic arguments led to estimates of $M_{\text{max}}^{\text{TOV}} \lesssim 2.1 - 2.3 M_{\odot}$ [82, 83, 84, 85]. Further, using empirical relations between NS radii and the threshold mass M_{pc} for prompt collapse it is possible to tentatively rule out EOS predicting minimal NS radii < 10 km and radii at $1.6 M_{\odot} \lesssim 11$ km

[196]. Combining the GW data and the phenomenological fit of the disc mass in Fig. 7 also leads to a possible lower bound on the tidal parameter and thus a stronger constraint on the tidal parameter $300 \lesssim \tilde{\Lambda} \lesssim 800$ [37, 119].

GW190425 is associated to the heaviest BNS source known to date with $M \simeq 3.2 - 3.7 M_{\odot}$ [14]. The mass ratio of GW190425 can be as high as $q \sim 1.25$ ($q \sim 2.5$) for low (high) spin priors. Using the NR prompt collapse models presented in Sec. 3, it is possible to estimate that the probability for the remnant of GW190425 to promptly collapse to BH is $\sim 97\%$ [14]. For an equal mass merger ($q \sim 1$), a prompt collapse does not form a significant disc (Sec. 6) and thus no bright electromagnetic counterparts would be expected from this event, e.g. [207]. However, the conclusions would be different in the scenario that GW190425 was produced by an asymmetric binary with $q \gtrsim 1.6$. The prompt collapse threshold significantly decreases for large q (Sec. 3) while massive neutron-rich discs are likely (Sec. 6). On the one hand, the prompt collapse to BH outcome is strengthened in the $q \gtrsim 1.6$ scenario. On the other hand, a bright and temporally extended red kilonova, similar to the one expected for BH-NS binaries, would have been an expected likely counterpart [28, 208, 78].

To conclude, the science outcomes of BNS mergers observations will crucially depend on the quantitative characterization of the merger outcome. While numerical-relativity efforts towards physically realistic and quantitative models for multimessenger analysis are ongoing, the interplay between theory, simulations and observations appears necessary to guide these efforts.

Acknowledgements The author thanks M. Breschi, B. Giacomazzo, A. Perego, D. Radice, F. Schianchi, F. Zappa for discussions, comments and help with the manuscript, as well as members of CoRe and of the Prometeo Virgo group for discussions and inputs. The author acknowledges support by the EU H2020 under ERC Starting Grant, no. BinGraSp-714626.

A Numerical-relativity methods

Numerical-relativity simulations are based on the 3+1 formalism of general relativity [209, 210, 211]. This appendix schematically summarizes the main physics and techniques implemented in current state-of-art simulations.

- *Initial data* for circular merger simulation are prepared by solving the constraint equations of 3+1 general relativity in presence of a helical Killing vector and under the assumption of a conformally flat metric [212]. The EOS used for the initial data are polytropes or constructed from the minimum temperature slice of the EOS table employed for the evolution assuming neutrino-less beta-equilibrium. Consistent initial data for circular merger with NS with spinning are constructed with an extension of the formalism that is suitable for a constant rotation velocity of the NS [213, 214].
- *Einstein equations* are then solved with free-evolution schemes like BSSNOK [215, 216, 217] or the Z4c [218, 219, 220] based on the conformal decomposition of the metric fields. The latter scheme (and variation on the original proposal [221, 222, 223]) incorporate better constraint propagation and damping properties with respect to BSSN and is thus preferable to BSSN in nonvacuum spacetimes. Neutron star spacetime evolution are also performed with the generalized harmonic scheme [224].
- *Gauge conditions* are chosen as 1+log and Gamma-driver shift similarly to binary black hole simulations [225, 226, 227, 228, 229]. These conditions handle the singularities formation and movement as moving punctures [230, 231, 232].

- *General relativistic magnetohydrodynamics* is treated in conservative form [233]. Finite volume methods are typically employed to solve the hydrodynamics; high-order reconstructions or shock-capturing finite differencing schemes proved to be important for waveform modeling [74, 234, 235]. Magnetohydrodynamics is handled using constraint-transport schemes to control the magnetic-field-divergence [236, 237, 141, 238, 239, 240]. Nonideal (resistive) magnetohydrodynamics schemes have been formulated in general relativity although their applications to mergers have been limited to date [241, 242].
- Approximate *neutrino transport schemes* are based on the leakage scheme in the optically thick regions [243, 154, 244]. If considered, free-streaming neutrinos are treated with the M1 closure scheme [117, 112] or with the M0 scheme [30]. The latter is a simplified but computationally efficient scheme free of the radiation shock artifact that plagues the M1 scheme [189].
- *Equations of state* models simulated so far include Skyrme models with finite-temperature and composition dependency, e.g. the LS220 [245] and the SLy4 [246, 247]; relativistic mean field models [248] with temperature and composition dependencies like the DD2 [249, 250] and the SFHo [251]; and Brueckner-Hartree-Fock extensions to finite temperature like the BLh [252]. Softening effects at extreme densities have been simulated with EOS with Λ -hyperons like the Shen H. et al. [253] and the BHB $\Lambda\phi$ [254], or with quark-deconfinement transitions implemented by relativistic mean field models combined with bag models. Large samples of piecewise polytropic EOS [255] or cold/beta-equilibrated microphysical with a thermal pressure contribution given by a I -law have been simulated by various groups. Most of these EOS are compatible with present nuclear constraints and the cold, neutrino-less β -equilibrated matter predicts NS maximum masses and radii within the range allowed by current astrophysical constraints, including the recent GW constraints.
- *General-relativistic viscous hydrodynamics* schemes have been developed recently. One method is the general-relativistic large eddy simulations method (GRLES) [146]. Another method is based on a simplified Israel-Stewart formalism of general-relativistic shear-viscous hydrodynamics [147, 256]. Both approaches simulate turbulent viscosity by specifying an effective shear parameter $\nu \propto c_s$ (where c_s is the sound speed) that sets the intensity of the turbulence.
- The *computational domain* is typically covered by a structured grid composed of Cartesian overlapping domains (box-in-box) with 2:1 mesh refinement between parent and child. Evolutions are performed with method of line and the Berger-Oliger algorithm with sub-cycling in time and refluxing [257, 258]. The computational domain covers from the interior of the stars to the radiation zone, with the possibility of moving some of the Cartesian boxes to follow the orbital motion. An outer spherical grid composed of multipatches is sometimes used to extend the radiation zone [259, 260]. Spherical grids are being explored and could help for long-term simulations of the postmerger phase [223].
- *Gravitational waves* are extracted on coordinate sphere at large radii using metric (Regge-Wheeler-Zerilli) or curvature (Newmann-Penrose) perturbation theory of spherical or axisymmetric spacetimes [261, 262, 263].
- *Mass ejecta* are computed as those fluid elements that satisfy either the geodesic criterion, $-u_t > 1$ where u^μ is the fluid's 4-velocity, or the Bernoulli criterion, $-hu_t > 1$ where $h \geq 1$ is the enthalpy, on large-radii extraction spheres. Both criteria are approximated. The former criterion assumes the ejecta's fluid elements are on ballistic trajectories and neglects the fluids pressure. The latter criterion strictly applies to steady-stateflow $[(\partial_t)^\alpha$ is Killing vector]. The geodesic criterion is usually adopted for the fast dynamical ejecta while the Bernoulli one is employed for the winds.
- *Black-hole horizon* and properties are computed using apparent horizons [264].

Publicly available NR datasets from merger simulations exist and will be significantly growing in the next years. Gravitational waveforms for hundreds of configurations have been released by the CoRe collaboration [79], the MPI/Kyoto group [265] and the SXS collaboration [266] on their websites ⁸ Ejecta data from the CoRe collaboration [30] are available on **Zenodo**

⁸ <http://www.computational-relativity.org/>
http://www2.yukawa.kyoto-u.ac.jp/~nr_kyoto/SACRA_PUB/catalog.html
<https://data.black-holes.org/waveforms/index.html>

[267]. There exists a **Zenodo** community called *NRGW open data* that hosts a collection of datasets from numerical relativity and gravitational waves modeling papers:

<https://zenodo.org/communities/nrgw-opendata/>

Data upload and download are open and welcome.

References

1. B.P. Abbott, et al., Phys. Rev. Lett. **119**(16), 161101 (2017). DOI 10.1103/PhysRevLett.119.161101
2. B.P. Abbott, et al., Phys. Rev. **X9**(1), 011001 (2019). DOI 10.1103/PhysRevX.9.011001
3. B.P. Abbott, et al., Phys. Rev. **X9**(3), 031040 (2019). DOI 10.1103/PhysRevX.9.031040
4. T. Damour, A. Nagar, L. Villain, Phys.Rev. **D85**, 123007 (2012). DOI 10.1103/PhysRevD.85.123007
5. M. Favata, Phys.Rev.Lett. **112**, 101101 (2014). DOI 10.1103/PhysRevLett.112.101101
6. W. Del Pozzo, T.G.F. Li, M. Agathos, C. Van Den Broeck, S. Vitale, Phys. Rev. Lett. **111**(7), 071101 (2013). DOI 10.1103/PhysRevLett.111.071101
7. B.P. Abbott, et al., Phys. Rev. Lett. **121**(16), 161101 (2018). DOI 10.1103/PhysRevLett.121.161101
8. D. Lai, S.L. Shapiro, Astrophys. J. **442**, 259 (1995). DOI 10.1086/175438
9. C. Cutler, Phys. Rev. **D66**, 084025 (2002). DOI 10.1103/PhysRevD.66.084025
10. A. Corsi, P. Mszros, Astrophys. J. **702**, 1171 (2009). DOI 10.1088/0004-637X/702/2/1171
11. S. Dall’Osso, B. Giacomazzo, R. Perna, L. Stella, Astrophys. J. **798**(1), 25 (2015). DOI 10.1088/0004-637X/798/1/25
12. P.D. Lasky, K. Glampedakis, Mon. Not. Roy. Astron. Soc. **458**(2), 1660 (2016). DOI 10.1093/mnras/stw435
13. B.P. Abbott, et al., (2018). DOI 10.3847/1538-4357/ab0f3d
14. B.P. Abbott, et al., (2020)
15. M. Shibata, K. Uryu, Phys. Rev. **D61**, 064001 (2000). DOI 10.1103/PhysRevD.61.064001
16. M. Shibata, K. Uryu, Prog. Theor. Phys. **107**, 265 (2002). DOI 10.1143/PTP.107.265
17. M. Anderson, E.W. Hirschmann, L. Lehner, S.L. Liebling, P.M. Motl, et al., Phys.Rev. **D77**, 024006 (2008). DOI 10.1103/PhysRevD.77.024006
18. L. Baiotti, B. Giacomazzo, L. Rezzolla, Phys. Rev. **D78**, 084033 (2008). DOI 10.1103/PhysRevD.78.084033
19. K. Hotokezaka, K. Kyutoku, H. Okawa, M. Shibata, K. Kiuchi, Phys.Rev. **D83**, 124008 (2011). DOI 10.1103/PhysRevD.83.124008
20. A. Bauswein, T. Baumgarte, H.T. Janka, Phys.Rev.Lett. **111**(13), 131101 (2013). DOI 10.1103/PhysRevLett.111.131101
21. N. Stergioulas, A. Bauswein, K. Zagkouris, H.T. Janka, Mon.Not.Roy.Astron.Soc. **418**, 427 (2011). DOI 10.1111/j.1365-2966.2011.19493.x
22. A. Bauswein, H.T. Janka, Phys.Rev.Lett. **108**, 011101 (2012). DOI 10.1103/PhysRevLett.108.011101
23. K. Hotokezaka, K. Kiuchi, K. Kyutoku, T. Muranushi, Y.i. Sekiguchi, et al., Phys.Rev. **D88**(4), 044026 (2013). DOI 10.1103/PhysRevD.88.044026
24. K. Takami, L. Rezzolla, L. Baiotti, Phys.Rev.Lett. **113**, 091104 (2014). DOI 10.1103/PhysRevLett.113.091104
25. S. Bernuzzi, T. Dietrich, A. Nagar, Phys. Rev. Lett. **115**, 091101 (2015). DOI 10.1103/PhysRevLett.115.091101
26. Y. Sekiguchi, K. Kiuchi, K. Kyutoku, M. Shibata, Phys.Rev.Lett. **107**, 051102 (2011). DOI 10.1103/PhysRevLett.107.051102
27. A. Perego, S. Bernuzzi, D. Radice, Eur. Phys. J. **A55**(8), 124 (2019). DOI 10.1140/epja/i2019-12810-7

28. D. Radice, A. Perego, S. Bernuzzi, B. Zhang, *Mon. Not. Roy. Astron. Soc.* **481**(3), 3670 (2018). DOI 10.1093/mnras/sty2531
29. S. Fujibayashi, Y. Sekiguchi, K. Kiuchi, M. Shibata, *Astrophys. J.* **846**(2), 114 (2017). DOI 10.3847/1538-4357/aa8039
30. D. Radice, A. Perego, K. Hotokezaka, S.A. Fromm, S. Bernuzzi, L.F. Roberts, *Astrophys. J.* **869**(2), 130 (2018). DOI 10.3847/1538-4357/aaf054
31. K. Kiuchi, K. Kyutoku, M. Shibata, K. Taniguchi, *Astrophys. J.* **876**(2), L31 (2019). DOI 10.3847/2041-8213/ab1e45
32. R. Ciolfi, W. Kastaun, J.V. Kalinani, B. Giacomazzo, *Phys. Rev.* **D100**(2), 023005 (2019). DOI 10.1103/PhysRevD.100.023005
33. M. Shibata, K. Taniguchi, K. Uryu, *Phys. Rev.* **D68**, 084020 (2003). DOI 10.1103/PhysRevD.68.084020
34. M. Shibata, K. Taniguchi, *Phys.Rev.* **D73**, 064027 (2006). DOI 10.1103/PhysRevD.73.064027
35. K. Kiuchi, Y. Sekiguchi, M. Shibata, K. Taniguchi, *Phys. Rev.* **D80**, 064037 (2009). DOI 10.1103/PhysRevD.80.064037
36. L. Rezzolla, L. Baiotti, B. Giacomazzo, D. Link, J.A. Font, *Class. Quant. Grav.* **27**, 114105 (2010). DOI 10.1088/0264-9381/27/11/114105
37. D. Radice, A. Perego, F. Zappa, S. Bernuzzi, *Astrophys. J.* **852**(2), L29 (2018). DOI 10.3847/2041-8213/aaa402
38. R. Fernandez, B.D. Metzger, *Mon. Not. Roy. Astron. Soc.* **435**, 502 (2013). DOI 10.1093/mnras/stt1312
39. B.D. Metzger, R. Fernández, *Mon.Not.Roy.Astron.Soc.* **441**, 3444 (2014). DOI 10.1093/mnras/stu802
40. O. Just, A. Bauswein, R.A. Pulpillo, S. Goriely, H.T. Janka, *Mon. Not. Roy. Astron. Soc.* **448**(1), 541 (2015). DOI 10.1093/mnras/stv009
41. D.M. Siegel, R. Ciolfi, L. Rezzolla, *Astrophys. J.* **785**, L6 (2014). DOI 10.1088/2041-8205/785/1/L6
42. S. Fujibayashi, K. Kiuchi, N. Nishimura, Y. Sekiguchi, M. Shibata, *Astrophys. J.* **860**(1), 64 (2018). DOI 10.3847/1538-4357/aabafd
43. J.M. Lattimer, D.N. Schramm, *Astrophys. J.* **192**, L145 (1974). DOI 10.1086/181612
44. D. Eichler, M. Livio, T. Piran, D.N. Schramm, *Nature* **340**, 126 (1989). DOI 10.1038/340126a0
45. S. Wanajo, Y. Sekiguchi, N. Nishimura, K. Kiuchi, K. Kyutoku, M. Shibata, *Astrophys. J.* **789**, L39 (2014). DOI 10.1088/2041-8205/789/2/L39
46. S. Rosswog, *Int.J.Mod.Phys.* **D24**(05), 1530012 (2015). DOI 10.1142/S0218271815300128
47. D. Kasen, B. Metzger, J. Barnes, E. Quataert, E. Ramirez-Ruiz, *Nature* (2017). DOI 10.1038/nature24453. [Nature551,80(2017)]
48. J.J. Cowan, C. Sneden, J.E. Lawler, A. Aprahamian, M. Wiescher, K. Langanke, G. Martinez-Pinedo, F.K. Thielemann, (2019)
49. L.X. Li, B. Paczynski, *Astrophys.J.* **507**, L59 (1998). DOI 10.1086/311680
50. B. Metzger, G. Martinez-Pinedo, S. Darbha, E. Quataert, A. Arcones, et al., *Mon.Not.Roy.Astron.Soc.* **406**, 2650 (2010). DOI 10.1111/j.1365-2966.2010.16864.x
51. D. Kasen, N.R. Badnell, J. Barnes, *Astrophys. J.* **774**, 25 (2013). DOI 10.1088/0004-637X/774/1/25
52. M. Tanaka, K. Hotokezaka, *Astrophys.J.* **775**, 113 (2013). DOI 10.1088/0004-637X/775/2/113
53. B.D. Metzger, *Living Rev. Rel.* **23**(1), 1 (2020). DOI 10.1007/s41114-019-0024-0
54. S. Rosswog, M. Liebendoerfer, F. Thielemann, M. Davies, W. Benz, et al., *Astron.Astrophys.* **341**, 499 (1999)
55. K. Hotokezaka, K. Kiuchi, K. Kyutoku, H. Okawa, Y.i. Sekiguchi, et al., *Phys.Rev.* **D87**, 024001 (2013). DOI 10.1103/PhysRevD.87.024001
56. A. Bauswein, S. Goriely, H.T. Janka, *Astrophys.J.* **773**, 78 (2013). DOI 10.1088/0004-637X/773/1/78
57. W.H. Lee, E. Ramirez-Ruiz, Diego-Lopez-Camara, *Astrophys.J.* **699**, L93 (2009). DOI 10.1088/0004-637X/699/2/L93
58. R. Fernandez, B.D. Metzger, *Ann. Rev. Nucl. Part. Sci.* **66**, 23 (2016). DOI 10.1146/annurev-nucl-102115-044819

59. D.M. Siegel, B.D. Metzger, Phys. Rev. Lett. **119**(23), 231102 (2017). DOI 10.1103/PhysRevLett.119.231102
60. R. Fernández, A. Tchekhovskoy, E. Quataert, F. Foucart, D. Kasen, Mon. Not. Roy. Astron. Soc. **482**(3), 3373 (2019). DOI 10.1093/mnras/sty2932
61. F. Zappa, S. Bernuzzi, D. Radice, A. Perego, T. Dietrich, Phys. Rev. Lett. **120**(11), 111101 (2018). DOI 10.1103/PhysRevLett.120.111101
62. T. Damour, in *Gravitational Radiation*, ed. by N. Deruelle, T. Piran (North-Holland, Amsterdam, 1983), pp. 59–144
63. T. Damour, M. Soffel, C.m. Xu, Phys. Rev. **D43**, 3273 (1991). DOI 10.1103/PhysRevD.43.3273
64. T. Damour, M. Soffel, C.m. Xu, Phys. Rev. **D49**, 618 (1994). DOI 10.1103/PhysRevD.49.618
65. E. Racine, E.E. Flanagan, Phys. Rev. **D71**, 044010 (2005). DOI 10.1103/PhysRevD.71.044010, 10.1103/PhysRevD.88.089903. [Erratum: Phys. Rev.D88,no.8,089903(2013)]
66. T. Damour, A. Nagar, Phys. Rev. **D81**, 084016 (2010). DOI 10.1103/PhysRevD.81.084016
67. T. Hinderer, Astrophys.J. **677**, 1216 (2008). DOI 10.1086/533487
68. T. Damour, A. Nagar, Phys. Rev. **D80**, 084035 (2009). DOI 10.1103/PhysRevD.80.084035
69. T. Binnington, E. Poisson, Phys. Rev. **D80**, 084018 (2009). DOI 10.1103/PhysRevD.80.084018
70. E.E. Flanagan, T. Hinderer, Phys.Rev. **D77**, 021502 (2008). DOI 10.1103/PhysRevD.77.021502
71. S. Bernuzzi, D. Radice, C.D. Ott, L.F. Roberts, P. Moesta, F. Galeazzi, Phys. Rev. **D94**(2), 024023 (2016). DOI 10.1103/PhysRevD.94.024023
72. M. Breschi, S. Bernuzzi, F. Zappa, M. Agathos, A. Perego, D. Radice, A. Nagar, Phys. Rev. **D100**(10), 104029 (2019). DOI 10.1103/PhysRevD.100.104029
73. T. Damour, A. Nagar, D. Pollney, C. Reisswig, Phys.Rev.Lett. **108**, 131101 (2012). DOI 10.1103/PhysRevLett.108.131101
74. S. Bernuzzi, A. Nagar, M. Thierfelder, B. Brügmann, Phys.Rev. **D86**, 044030 (2012). DOI 10.1103/PhysRevD.86.044030
75. S. Bernuzzi, A. Nagar, S. Balmelli, T. Dietrich, M. Ujevic, Phys.Rev.Lett. **112**, 201101 (2014). DOI 10.1103/PhysRevLett.112.201101
76. S. Bernuzzi, A. Nagar, T. Dietrich, T. Damour, Phys.Rev.Lett. **114**(16), 161103 (2015). DOI 10.1103/PhysRevLett.114.161103
77. S. Bernuzzi, T. Dietrich, W. Tichy, B. Brügmann, Phys.Rev. **D89**, 104021 (2014). DOI 10.1103/PhysRevD.89.104021
78. S. Bernuzzi, et al., (2020)
79. T. Dietrich, D. Radice, S. Bernuzzi, F. Zappa, A. Perego, B. Brügmann, S.V. Chaurasia, R. Dudi, W. Tichy, M. Ujevic, Class. Quant. Grav. **35**(24), 24LT01 (2018). DOI 10.1088/1361-6382/aaebc0
80. S. Koepfel, L. Bovard, L. Rezzolla, Astrophys. J. **872**(1), L16 (2019). DOI 10.3847/2041-8213/ab0210
81. M. Agathos, F. Zappa, S. Bernuzzi, A. Perego, M. Breschi, D. Radice, Phys. Rev. **D101**(4), 044006 (2020). DOI 10.1103/PhysRevD.101.044006
82. B. Margalit, B.D. Metzger, Astrophys. J. **850**(2), L19 (2017). DOI 10.3847/2041-8213/aa991c
83. M. Shibata, S. Fujibayashi, K. Hotokezaka, K. Kiuchi, K. Kyutoku, Y. Sekiguchi, M. Tanaka, Phys. Rev. **D96**(12), 123012 (2017). DOI 10.1103/PhysRevD.96.123012
84. L. Rezzolla, E.R. Most, L.R. Weih, Astrophys. J. **852**(2), L25 (2018). DOI 10.3847/2041-8213/aaa401
85. M. Ruiz, S.L. Shapiro, A. Tsokaros, Phys. Rev. **D97**(2), 021501 (2018). DOI 10.1103/PhysRevD.97.021501
86. A. Bauswein, S. Blacker, V. Vijayan, N. Stergioulas, K. Chatziioannou, J.A. Clark, N.U.F. Bastian, D.B. Blaschke, M. Cierniak, T. Fischer, (2020)
87. W. Kastaun, F. Galeazzi, D. Alic, L. Rezzolla, J.A. Font, Phys.Rev. **D88**, 021501 (2013). DOI 10.1103/PhysRevD.88.021501
88. T. Dietrich, S. Bernuzzi, M. Ujevic, W. Tichy, Phys. Rev. **D95**(4), 044045 (2017). DOI 10.1103/PhysRevD.95.044045

89. K. Kiuchi, Y. Sekiguchi, M. Shibata, K. Taniguchi, *Phys. Rev. Lett.* **104**, 141101 (2010). DOI 10.1103/PhysRevLett.104.141101
90. T. Dietrich, M. Ujevic, W. Tichy, S. Bernuzzi, B. Brügmann, *Phys. Rev.* **D95**(2), 024029 (2017). DOI 10.1103/PhysRevD.95.024029
91. J.M. Bardeen, *Nature* **226**, 64 (1970)
92. K.S. Thorne, *Astrophys. J.* **191**, 507 (1974). DOI 10.1086/152991
93. C.F. Gammie, S.L. Shapiro, J.C. McKinney, *Astrophys. J.* **602**, 312 (2004). DOI 10.1086/380996
94. R. Narayan, I.V. Igumenshchev, M.A. Abramowicz, *Publ. Astron. Soc. Jap.* **55**, L69 (2003). DOI 10.1093/pasj/55.6.L69
95. A. Tchekhovskoy, R. Narayan, J.C. McKinney, *Mon. Not. Roy. Astron. Soc.* **418**(1), L79 (2011). DOI 10.1111/j.1745-3933.2011.01147.x
96. W.H. Lee, E. Ramirez-Ruiz, D. Page, *Astrophys. J.* **632**, 421 (2005). DOI 10.1086/432373
97. I.M. Christie, A. Lalakos, A. Tchekhovskoy, R. Fernández, F. Foucart, E. Quataert, D. Kasen, (2019)
98. D.M. Siegel, B.D. Metzger, *Astrophys. J.* **858**(1), 52 (2018). DOI 10.3847/1538-4357/aaabac
99. A.J. Benson, A. Babul, *Mon. Not. Roy. Astron. Soc.* **397**(3), 1302 (2009). DOI 10.1111/j.1365-2966.2009.15087.x
100. I. Zalamea, A.M. Beloborodov, *Mon. Not. Roy. Astron. Soc.* **410**, 2302 (2011). DOI 10.1111/j.1365-2966.2010.17600.x
101. E. Nakar, *Phys. Rept.* **442**, 166 (2007). DOI 10.1016/j.physrep.2007.02.005
102. R.D. Blandford, R.L. Znajek, *Mon. Not. Roy. Astron. Soc.* **179**, 433 (1977). DOI 10.1093/mnras/179.3.433
103. J. Antoniadis, P.C. Freire, N. Wex, T.M. Tauris, R.S. Lynch, et al., *Science* **340**, 6131 (2013). DOI 10.1126/science.1233232
104. H.T. Cromartie, et al., *Nat. Astron.* **4**(1), 72 (2019). DOI 10.1038/s41550-019-0880-2
105. T.W. Baumgarte, S.L. Shapiro, M. Shibata, *Astrophys. J.* **528**, L29 (2000)
106. G.B. Cook, S.L. Shapiro, S.A. Teukolsky, *Astrophys. J.* **398**, 203 (1992). DOI 10.1086/171849
107. G.B. Cook, S.L. Shapiro, S.A. Teukolsky, *Astrophys. J.* **424**, 823 (1994). DOI 10.1086/173934
108. W. Kastaun, R. Ciolfi, B. Giacomazzo, *Phys. Rev. D* **94**(4), 044060 (2016). DOI 10.1103/PhysRevD.94.044060
109. M. Ruffert, H. Janka, K. Takahashi, G. Schäfer, *Astron.Astrophys.* **319**, 122 (1997)
110. C. Palenzuela, S.L. Liebling, D. Neilsen, L. Lehner, O.L. Caballero, E. O'Connor, M. Anderson, *Phys. Rev.* **D92**(4), 044045 (2015). DOI 10.1103/PhysRevD.92.044045
111. F. Foucart, R. Haas, M.D. Duez, E. O'Connor, C.D. Ott, L. Roberts, L.E. Kidder, J. Lippuner, H.P. Pfeiffer, M.A. Scheel, *Phys. Rev.* **D93**(4), 044019 (2016). DOI 10.1103/PhysRevD.93.044019
112. F. Foucart, E. O'Connor, L. Roberts, L.E. Kidder, H.P. Pfeiffer, M.A. Scheel, *Phys. Rev.* **D94**(12), 123016 (2016). DOI 10.1103/PhysRevD.94.123016
113. A. Endrizzi, A. Perego, F.M. Fabbri, L. Branca, D. Radice, S. Bernuzzi, B. Giacomazzo, F. Pederiva, A. Lovato, *Eur.Phys.J.A* **56**(1), 15 (2020). DOI 10.1140/epja/s10050-019-00018-6
114. A. Perego, S. Rosswog, R. Cabezon, O. Korobkin, R. Kaeppeli, et al., *Mon.Not.Roy.Astron.Soc.* **443**, 3134 (2014). DOI 10.1093/mnras/stu1352
115. S. Goriely, A. Bauswein, O. Just, E. Pllumbi, H.T. Janka, *Mon. Not. Roy. Astron. Soc.* **452**(4), 3894 (2015). DOI 10.1093/mnras/stv1526
116. D. Radice, F. Galeazzi, J. Lippuner, L.F. Roberts, C.D. Ott, L. Rezzolla, *Mon. Not. Roy. Astron. Soc.* **460**(3), 3255 (2016). DOI 10.1093/mnras/stw1227
117. Y. Sekiguchi, K. Kiuchi, K. Kyutoku, M. Shibata, K. Taniguchi, *Phys. Rev.* **D93**(12), 124046 (2016). DOI 10.1103/PhysRevD.93.124046
118. D. Martin, A. Perego, W. Kastaun, A. Arcones, *Class. Quant. Grav.* **35**(3), 034001 (2018). DOI 10.1088/1361-6382/aa9f5a
119. D. Radice, L. Dai, *Eur. Phys. J.* **A55**(4), 50 (2019). DOI 10.1140/epja/i2019-12716-4
120. Y. Sekiguchi, K. Kiuchi, K. Kyutoku, M. Shibata, *Phys.Rev.Lett.* **107**, 211101 (2011). DOI 10.1103/PhysRevLett.107.211101

121. D. Radice, S. Bernuzzi, W. Del Pozzo, L.F. Roberts, C.D. Ott, *Astrophys. J.* **842**(2), L10 (2017). DOI 10.3847/2041-8213/aa775f
122. A. Bauswein, N.U.F. Bastian, D.B. Blaschke, K. Chatziioannou, J.A. Clark, T. Fischer, M. Oertel, *Phys. Rev. Lett.* **122**(6), 061102 (2019). DOI 10.1103/PhysRevLett.122.061102
123. E.R. Most, L.J. Papenfort, V. Dexheimer, M. Hanauske, S. Schramm, H. Stcker, L. Rezzolla, *Phys. Rev. Lett.* **122**(6), 061101 (2019). DOI 10.1103/PhysRevLett.122.061101
124. A. Bauswein, H. Janka, K. Hebeler, A. Schwenk, *Phys.Rev.* **D86**, 063001 (2012). DOI 10.1103/PhysRevD.86.063001
125. D. Radice, S. Bernuzzi, C.D. Ott, *Phys. Rev.* **D94**(6), 064011 (2016). DOI 10.1103/PhysRevD.94.064011
126. L. Lehner, S.L. Liebling, C. Palenzuela, O.L. Caballero, E. O'Connor, M. Anderson, D. Neilsen, *Class. Quant. Grav.* **33**(18), 184002 (2016). DOI 10.1088/0264-9381/33/18/184002
127. A. Bauswein, N. Stergioulas, H.T. Janka, *Phys.Rev.* **D90**(2), 023002 (2014). DOI 10.1103/PhysRevD.90.023002
128. L. Lehner, S.L. Liebling, C. Palenzuela, P.M. Motl, *Phys. Rev.* **D94**(4), 043003 (2016). DOI 10.1103/PhysRevD.94.043003
129. L. Rezzolla, K. Takami, *Phys. Rev.* **D93**(12), 124051 (2016). DOI 10.1103/PhysRevD.93.124051
130. K. Kiuchi, K. Kyohei, K. Kyutoku, Y. Sekiguchi, M. Shibata, (2019)
131. A. Bauswein, N. Stergioulas, H.T. Janka, *Eur. Phys. J.* **A52**(3), 56 (2016). DOI 10.1140/epja/i2016-16056-7
132. S. Bose, K. Chakravarti, L. Rezzolla, B.S. Sathyaprakash, K. Takami, *Phys. Rev. Lett.* **120**(3), 031102 (2018). DOI 10.1103/PhysRevLett.120.031102
133. K.W. Tsang, T. Dietrich, C. Van Den Broeck, *Phys. Rev.* **D100**(4), 044047 (2019). DOI 10.1103/PhysRevD.100.044047
134. A.W. Steiner, J.M. Lattimer, E.F. Brown, *Eur. Phys. J.* **A52**(2), 18 (2016). DOI 10.1140/epja/i2016-16018-1
135. A. Torres-Rivas, K. Chatziioannou, A. Bauswein, J.A. Clark, *Phys. Rev.* **D99**(4), 044014 (2019). DOI 10.1103/PhysRevD.99.044014
136. N. Stergioulas, J.L. Friedman, *Astrophys. J.* **444**, 306 (1995). DOI 10.1086/175605
137. J. Kaplan, C. Ott, E. O'Connor, K. Kiuchi, L. Roberts, et al., *Astrophys.J.* **790**, 19 (2014). DOI 10.1088/0004-637X/790/1/19
138. M. Bocquet, S. Bonazzola, E. Gourgoulhon, J. Novak, *Astron. Astrophys.* **301**, 757 (1995)
139. M.D. Duez, Y.T. Liu, S.L. Shapiro, M. Shibata, *Phys. Rev.* **D73**, 104015 (2006). DOI 10.1103/PhysRevD.73.104015
140. M. Anderson, E.W. Hirschmann, L. Lehner, S.L. Liebling, P.M. Motl, et al., *Phys.Rev.Lett.* **100**, 191101 (2008). DOI 10.1103/PhysRevLett.100.191101
141. B. Giacomazzo, L. Rezzolla, L. Baiotti, *Phys. Rev.* **D83**, 044014 (2011). DOI 10.1103/PhysRevD.83.044014
142. K. Kiuchi, K. Kyutoku, Y. Sekiguchi, M. Shibata, *Phys. Rev.* **D97**(12), 124039 (2018). DOI 10.1103/PhysRevD.97.124039
143. M. Ruiz, A. Tsokaros, S.L. Shapiro, *Phys. Rev. D* **101**(6), 064042 (2020). DOI 10.1103/PhysRevD.101.064042
144. K. Kiuchi, P. Cerd-Durn, K. Kyutoku, Y. Sekiguchi, M. Shibata, *Phys. Rev. D* **92**(12), 124034 (2015). DOI 10.1103/PhysRevD.92.124034
145. N.I. Shakura, R.A. Sunyaev, *Astron. Astrophys.* **24**, 337 (1973)
146. D. Radice, *Astrophys. J.* **838**(1), L2 (2017). DOI 10.3847/2041-8213/aa6483
147. M. Shibata, K. Kiuchi, *Phys. Rev.* **D95**(12), 123003 (2017). DOI 10.1103/PhysRevD.95.123003
148. W. Kastaun, F. Galeazzi, *Phys.Rev.* **D91**(6), 064027 (2015). DOI 10.1103/PhysRevD.91.064027
149. A. Endrizzi, R. Ciolfi, B. Giacomazzo, W. Kastaun, T. Kawamura, *Class. Quant. Grav.* **33**(16), 164001 (2016). DOI 10.1088/0264-9381/33/16/164001
150. M. Hanauske, K. Takami, L. Bovard, L. Rezzolla, J.A. Font, F. Galeazzi, H. Stcker, *Phys. Rev. D* **96**(4), 043004 (2017). DOI 10.1103/PhysRevD.96.043004

151. R. Ciolfi, W. Kastaun, B. Giacomazzo, A. Endrizzi, D.M. Siegel, R. Perna, *Phys. Rev. D* **95**(6), 063016 (2017). DOI 10.1103/PhysRevD.95.063016
152. B.D. Metzger, T.A. Thompson, E. Quataert, *Astrophys. J.* **659**, 561 (2007). DOI 10.1086/512059
153. D.M. Siegel, R. Ciolfi, *Astrophys. J.* **819**(1), 14 (2016). DOI 10.3847/0004-637X/819/1/14
154. S. Rosswog, M. Liebendoerfer, *Mon.Not.Roy.Astron.Soc.* **342**, 673 (2003). DOI 10.1046/j.1365-8711.2003.06579.x
155. A. Burrows, T.J. Mazurek, J.M. Lattimer, *Astrophys. J.* **251**, 325 (1981). DOI 10.1086/159467
156. A. Burrows, J.M. Lattimer, *Astrophys. J.* **307**, 178 (1986). DOI 10.1086/164405
157. J. Pons, S. Reddy, M. Prakash, J. Lattimer, J. Miralles, *Astrophys. J.* **513**, 780 (1999). DOI 10.1086/306889
158. T. Fischer, S. Whitehouse, A. Mezzacappa, F.K. Thielemann, M. Liebendorfer, *Astron. Astrophys.* **517**, A80 (2010). DOI 10.1051/0004-6361/200913106
159. L.F. Roberts, S. Reddy, *Phys. Rev. C* **95**(4), 045807 (2017). DOI 10.1103/PhysRevC.95.045807
160. Y.Z. Fan, X.F. Wu, D.M. Wei, *Phys. Rev. D* **88**(6), 067304 (2013). DOI 10.1103/PhysRevD.88.067304
161. B. Gompertz, P. O'Brien, G. Wynn, A. Rowlinson, *Mon. Not. Roy. Astron. Soc.* **431**, 1745 (2013). DOI 10.1093/mnras/stt293
162. H. Gao, B. Zhang, H.J. L, *Phys. Rev. D* **93**(4), 044065 (2016). DOI 10.1103/PhysRevD.93.044065
163. J.L. Friedman, B.F. Schutz, *Astrophys. J.* **199**, L157 (1975). DOI 10.1086/181872
164. S. Chandrasekhar, *Phys. Rev. Lett.* **24**, 611 (1970). DOI 10.1103/PhysRevLett.24.611
165. N. Stergioulas, *Living Rev. Rel.* **6**, 3 (2003)
166. V. Paschalidis, W.E. East, F. Pretorius, S.L. Shapiro, *Phys. Rev. D* **92**(12), 121502 (2015). DOI 10.1103/PhysRevD.92.121502
167. W.E. East, V. Paschalidis, F. Pretorius, S.L. Shapiro, *Phys. Rev. D* **93**(2), 024011 (2016). DOI 10.1103/PhysRevD.93.024011
168. W.E. East, V. Paschalidis, F. Pretorius, *Class. Quant. Grav.* **33**(24), 244004 (2016). DOI 10.1088/0264-9381/33/24/244004
169. F. Foucart, T. Hinderer, S. Nissanke, *Phys. Rev. D* **98**(8), 081501 (2018). DOI 10.1103/PhysRevD.98.081501
170. F. Zappa, S. Bernuzzi, F. Pannarale, M. Mapelli, N. Giacobbo, *Phys. Rev. Lett.* **123**(4), 041102 (2019). DOI 10.1103/PhysRevLett.123.041102
171. A. Perego, H. Yasin, A. Arcones, *J. Phys. G* **44**(8), 084007 (2017). DOI 10.1088/1361-6471/aa7bdc
172. J.M. Miller, B.R. Ryan, J.C. Dolence, A. Burrows, C.J. Fontes, C.L. Fryer, O. Korobkin, J. Lippuner, M.R. Mumpower, R.T. Wollaeger, *Phys. Rev. D* **100**(2), 023008 (2019). DOI 10.1103/PhysRevD.100.023008
173. N. Bucciantini, B. Metzger, T. Thompson, E. Quataert, *Mon. Not. Roy. Astron. Soc.* **419**, 1537 (2012). DOI 10.1111/j.1365-2966.2011.19810.x
174. M. Ruiz, R.N. Lang, V. Paschalidis, S.L. Shapiro, *Astrophys. J.* **824**(1), L6 (2016). DOI 10.3847/2041-8205/824/1/L6
175. P. Msta, D. Radice, R. Haas, E. Schnetter, S. Bernuzzi, (2020)
176. B.D. Metzger, T.A. Thompson, E. Quataert, *Astrophys. J.* **856**(2), 101 (2018). DOI 10.3847/1538-4357/aab095
177. M. Shibata, K. Hotokezaka, *Ann. Rev. Nucl. Part. Sci.* **69**, 41 (2019). DOI 10.1146/annurev-nucl-101918-023625
178. S. Rosswog, J. Sollerman, U. Feindt, A. Goobar, O. Korobkin, R. Wollaeger, C. Fremling, M.M. Kasliwal, *Astron. Astrophys.* **615**, A132 (2018). DOI 10.1051/0004-6361/201732117
179. A. Perego, D. Radice, S. Bernuzzi, *Astrophys. J.* **850**(2), L37 (2017). DOI 10.3847/2041-8213/aa9ab9
180. V. Nedora, S. Bernuzzi, D. Radice, A. Perego, A. Endrizzi, N. Ortiz, *Astrophys. J.* **886**(2), L30 (2019). DOI 10.3847/2041-8213/ab5794
181. Y. Sekiguchi, K. Kiuchi, K. Kyutoku, M. Shibata, *Phys.Rev. D* **91**(6), 064059 (2015). DOI 10.1103/PhysRevD.91.064059

182. L. Bovard, D. Martin, F. Guercilena, A. Arcones, L. Rezzolla, O. Korobkin, *Phys. Rev. D* **96**(12), 124005 (2017). DOI 10.1103/PhysRevD.96.124005
183. T. Vincent, F. Foucart, M.D. Duez, R. Haas, L.E. Kidder, H.P. Pfeiffer, M.A. Scheel, *Phys. Rev. D* **101**(4), 044053 (2020). DOI 10.1103/PhysRevD.101.044053
184. T. Dietrich, M. Ujevic, *Class. Quant. Grav.* **34**(10), 105014 (2017). DOI 10.1088/1361-6382/aa6bb0
185. D. Radice, A. Perego, K. Hotokezaka, S. Bernuzzi, S.A. Fromm, L.F. Roberts, *Astrophys. J. Lett.* **869**, L35 (2018). DOI 10.3847/2041-8213/aaf053
186. K. Kawaguchi, K. Kyutoku, M. Shibata, M. Tanaka, *Astrophys. J.* **825**(1), 52 (2016). DOI 10.3847/0004-637X/825/1/52
187. E.R. Most, L.J. Papenfort, A. Tsokaros, L. Rezzolla, *Astrophys. J.* **884**, 40 (2019). DOI 10.3847/1538-4357/ab3ebb
188. L. Dessart, C. Ott, A. Burrows, S. Rosswog, E. Livne, *Astrophys. J.* **690**, 1681 (2009). DOI 10.1088/0004-637X/690/2/1681
189. F. Foucart, M.D. Duez, L.E. Kidder, R. Nguyen, H.P. Pfeiffer, M.A. Scheel, *Phys. Rev. D* **98**(6), 063007 (2018). DOI 10.1103/PhysRevD.98.063007
190. A.M. Beloborodov, *AIP Conf. Proc.* **1054**, 51 (2008). DOI 10.1063/1.3002509
191. S. Fahlman, R. Fernández, *Astrophys. J.* **869**(1), L3 (2018). DOI 10.3847/2041-8213/aaflab
192. J. Lippuner, L.F. Roberts, *Astrophys. J.* **815**(2), 82 (2015). DOI 10.1088/0004-637X/815/2/82
193. B.P. Abbott, et al., *Astrophys. J.* **848**(2), L12 (2017). DOI 10.3847/2041-8213/aa91c9
194. B.P. Abbott, et al., *Astrophys. J.* **851**(1), L16 (2017). DOI 10.3847/2041-8213/aa9a35
195. D. Martynov, et al., *Phys. Rev. D* **99**(10), 102004 (2019). DOI 10.1103/PhysRevD.99.102004
196. A. Bauswein, O. Just, H.T. Janka, N. Stergioulas, *Astrophys. J.* **850**(2), L34 (2017). DOI 10.3847/2041-8213/aa9994
197. P.S. Cowperthwaite, et al., *Astrophys. J.* **848**(2), L17 (2017). DOI 10.3847/2041-8213/aa8fc7
198. V.A. Villar, et al., *Astrophys. J.* **851**(1), L21 (2017). DOI 10.3847/2041-8213/aa9c84
199. N.R. Tanvir, et al., *Astrophys. J.* **848**, L27 (2017). DOI 10.3847/2041-8213/aa90b6
200. M. Tanaka, et al., *Publ. Astron. Soc. Jap.* (2017). DOI 10.1093/pasj/psx121
201. J. Lippuner, R. Fernández, L.F. Roberts, F. Foucart, D. Kasen, B.D. Metzger, C.D. Ott, *Mon. Not. Roy. Astron. Soc.* **472**(1), 904 (2017). DOI 10.1093/mnras/stx1987
202. K. Kawaguchi, M. Shibata, M. Tanaka, *Astrophys. J.* **865**(2), L21 (2018). DOI 10.3847/2041-8213/aade02
203. D. Lazzati, A. Deich, B.J. Morsony, J.C. Workman, *Mon. Not. Roy. Astron. Soc.* **471**(2), 1652 (2017). DOI 10.1093/mnras/stx1683
204. O. Bromberg, A. Tchekhovskoy, O. Gottlieb, E. Nakar, T. Piran, *Mon. Not. Roy. Astron. Soc.* **475**(3), 2971 (2018). DOI 10.1093/mnras/stx3316
205. A.L. Piro, J.A. Kollmeier, (2017)
206. P.C. Duffell, E. Quataert, D. Kasen, H. Klion, *Astrophys. J.* **866**(1), 3 (2018). DOI 10.3847/1538-4357/aae084
207. R.J. Foley, D.A. Coulter, C.D. Kilpatrick, A.L. Piro, E. Ramirez-Ruiz, J. Schwab, (2020)
208. K. Kyutoku, S. Fujibayashi, K. Hayashi, K. Kawaguchi, K. Kiuchi, M. Shibata, M. Tanaka, *Astrophys. J.* **890**(1), L4 (2020). DOI 10.3847/2041-8213/ab6e70
209. E. Gourgoulhon, (2007)
210. M. Alcubierre, *Introduction to 3+1 Numerical Relativity* (Oxford University Press, 2008)
211. T. Baumgarte, S. Shapiro, *Numerical Relativity* (Cambridge University Press, Cambridge, 2010)
212. E. Gourgoulhon, P. Grandclement, K. Taniguchi, J.A. Marck, S. Bonazzola, *Phys. Rev. D* **63**, 064029 (2001). DOI 10.1103/PhysRevD.63.064029
213. W. Tichy, *Phys. Rev. D* **84**, 024041 (2011). DOI 10.1103/PhysRevD.84.024041
214. W. Tichy, *Phys. Rev. D* **86**, 064024 (2012). DOI 10.1103/PhysRevD.86.064024
215. T. Nakamura, K. Oohara, Y. Kojima, *Prog. Theor. Phys. Suppl.* **90**, 1 (1987)
216. M. Shibata, T. Nakamura, *Phys. Rev. D* **52**, 5428 (1995). DOI 10.1103/PhysRevD.52.5428

217. T.W. Baumgarte, S.L. Shapiro, Phys. Rev. **D59**, 024007 (1999). DOI 10.1103/PhysRevD.59.024007
218. C. Bona, T. Ledvinka, C. Palenzuela, M. Zacek, Phys. Rev. **D67**, 104005 (2003). DOI 10.1103/PhysRevD.67.104005
219. S. Bernuzzi, D. Hilditch, Phys. Rev. **D81**, 084003 (2010). DOI 10.1103/PhysRevD.81.084003
220. D. Hilditch, S. Bernuzzi, M. Thierfelder, Z. Cao, W. Tichy, B. Bruegmann, Phys. Rev. **D88**, 084057 (2013). DOI 10.1103/PhysRevD.88.084057
221. D. Alic, W. Kastaun, L. Rezzolla, Phys. Rev. **D88**(6), 064049 (2013). DOI 10.1103/PhysRevD.88.064049
222. M. Dumbser, F. Guercilena, S. Kppel, L. Rezzolla, O. Zanotti, Phys. Rev. **D97**(8), 084053 (2018). DOI 10.1103/PhysRevD.97.084053
223. V. Mewes, Y. Zlochower, M. Campanelli, T.W. Baumgarte, Z.B. Etienne, F.G.L. Ar-mengol, F. Cipolletta, (2020)
224. M.D. Duez, F. Foucart, L.E. Kidder, H.P. Pfeiffer, M.A. Scheel, S.A. Teukolsky, Phys. Rev. **D78**, 104015 (2008). DOI 10.1103/PhysRevD.78.104015
225. S. Brandt, B. Brügmann, Phys. Rev. Lett. **78**, 3606 (1997). DOI 10.1103/PhysRevLett.78.3606
226. J.G. Baker, J. Centrella, D.I. Choi, M. Koppitz, J. van Meter, Phys. Rev. Lett. **96**, 111102 (2006). DOI 10.1103/PhysRevLett.96.111102
227. M. Campanelli, C.O. Lousto, P. Marronetti, Y. Zlochower, Phys. Rev. Lett. **96**, 111101 (2006). DOI 10.1103/PhysRevLett.96.111101
228. J.R. van Meter, J.G. Baker, M. Koppitz, D.I. Choi, Phys. Rev. **D73**, 124011 (2006). DOI 10.1103/PhysRevD.73.124011
229. B. Brügmann, J.A. Gonzalez, M. Hannam, S. Husa, U. Sperhake, et al., Phys.Rev. **D77**, 024027 (2008). DOI 10.1103/PhysRevD.77.024027
230. L. Baiotti, L. Rezzolla, Phys. Rev. Lett. **97**, 141101 (2006). DOI 10.1103/PhysRevLett.97.141101
231. M. Thierfelder, S. Bernuzzi, D. Hilditch, B. Brügmann, L. Rezzolla, Phys.Rev. **D83**, 064022 (2011). DOI 10.1103/PhysRevD.83.064022
232. T. Dietrich, S. Bernuzzi, Phys.Rev. **D91**(4), 044039 (2015). DOI 10.1103/PhysRevD.91.044039
233. J.A. Font, Living Rev. Rel. **11**, 7 (2007)
234. D. Radice, L. Rezzolla, F. Galeazzi, Mon.Not.Roy.Astron.Soc. **437**, L46 (2014). DOI 10.1093/mnrasl/slt137
235. S. Bernuzzi, T. Dietrich, Phys. Rev. **D94**(6), 064062 (2016). DOI 10.1103/PhysRevD.94.064062
236. D.S. Balsara, Journal of Computational Physics **174**(2), 614 (2001). DOI 10.1006/jcph.2001.6917. URL <http://www.sciencedirect.com/science/article/pii/S0021999101969177>
237. L. Del Zanna, O. Zanotti, N. Bucciantini, P. Londrillo, Astron. Astrophys. **473**, 11 (2007). DOI 10.1051/0004-6361:20077093
238. Z.B. Etienne, V. Paschalidis, Y.T. Liu, S.L. Shapiro, Phys.Rev. **D85**, 024013 (2012). DOI 10.1103/PhysRevD.85.024013
239. P. Msta, B.C. Mundim, J.A. Faber, R. Haas, S.C. Noble, et al., Class.Quant.Grav. **31**, 015005 (2014). DOI 10.1088/0264-9381/31/1/015005
240. K. Kiuchi, K. Kyutoku, Y. Sekiguchi, M. Shibata, T. Wada, Phys.Rev. **D90**(4), 041502 (2014). DOI 10.1103/PhysRevD.90.041502
241. C. Palenzuela, Mon. Not. Roy. Astron. Soc. **431**, 1853 (2013). DOI 10.1093/mnras/stt311
242. C. Palenzuela, L. Lehner, M. Ponce, S.L. Liebling, M. Anderson, et al., Phys.Rev.Lett. **111**, 061105 (2013). DOI 10.1103/PhysRevLett.111.061105
243. M.H. Ruffert, H.T. Janka, G. Schäfer, Astron. Astrophys. **311**, 532 (1996)
244. D. Neilsen, S.L. Liebling, M. Anderson, L. Lehner, E. OConnor, et al., Phys.Rev. **D89**(10), 104029 (2014). DOI 10.1103/PhysRevD.89.104029
245. J.M. Lattimer, F.D. Swesty, Nucl. Phys. **A535**, 331 (1991). DOI 10.1016/0375-9474(91)90452-C
246. F. Douchin, P. Haensel, Astron. Astrophys. **380**, 151 (2001)

247. A.S. Schneider, L.F. Roberts, C.D. Ott, *Phys. Rev.* **C96**(6), 065802 (2017). DOI 10.1103/PhysRevC.96.065802
248. M. Oertel, M. Hempel, T. Klöhn, S. Typel, *Rev. Mod. Phys.* **89**(1), 015007 (2017). DOI 10.1103/RevModPhys.89.015007
249. S. Typel, G. Ropke, T. Klöhn, D. Blaschke, H.H. Wolter, *Phys. Rev.* **C81**, 015803 (2010). DOI 10.1103/PhysRevC.81.015803
250. M. Hempel, J. Schaffner-Bielich, *Nucl. Phys.* **A837**, 210 (2010). DOI 10.1016/j.nuclphysa.2010.02.010
251. A.W. Steiner, M. Hempel, T. Fischer, *Astrophys. J.* **774**, 17 (2013). DOI 10.1088/0004-637X/774/1/17
252. I. Bombaci, D. Logoteta, *Astron. Astrophys.* **609**, A128 (2018). DOI 10.1051/0004-6361/201731604
253. H. Shen, H. Toki, K. Oyamatsu, K. Sumiyoshi, *Nucl. Phys.* **A637**, 435 (1998). DOI 10.1016/S0375-9474(98)00236-X
254. S. Banik, M. Hempel, D. Bandyopadhyay, *Astrophys. J. Suppl.* **214**(2), 22 (2014). DOI 10.1088/0067-0049/214/2/22
255. J.S. Read, B.D. Lackey, B.J. Owen, J.L. Friedman, *Phys. Rev.* **D79**, 124032 (2009). DOI 10.1103/PhysRevD.79.124032
256. M. Shibata, K. Kiuchi, Y. Sekiguchi, *Phys. Rev.* **D95**(8), 083005 (2017). DOI 10.1103/PhysRevD.95.083005
257. M.J. Berger, J. Olinger, *J. Comput. Phys.* **53**, 484 (1984)
258. M.J. Berger, P. Colella, *Journal of Computational Physics* **82**, 64 (1989). DOI 10.1016/0021-9991(89)90035-1
259. C. Ronchi, R. Iacono, P. Paolucci, *Journal of Computational Physics* **124**(1), 93 (1996). DOI 10.1006/jcph.1996.0047. URL <http://www.sciencedirect.com/science/article/pii/S0021999196900479>
260. D. Pollney, C. Reisswig, E. Schnetter, N. Dorband, P. Diener, *Phys. Rev.* **D83**, 044045 (2011). DOI 10.1103/PhysRevD.83.044045
261. V. Moncrief, *Ann. Phys.* **88**, 323 (1974)
262. V. Moncrief, *Ann. Phys.* **88**(2), 343 (1974). DOI DOI:10.1016/0003-4916(74)90174-2. URL <http://www.sciencedirect.com/science/article/B6WB1-4DF50YP-17X/2/4ba3285675415ec3032a6e60ae6dd290>
263. S. Teukolsky, *Phys. Rev. Lett.* **29**, 1114 (1972). DOI 10.1103/PhysRevLett.29.1114
264. J. Thornburg, *Class. Quant. Grav.* **21**, 743 (2004). DOI 10.1088/0264-9381/21/2/026
265. K. Kiuchi, K. Kawaguchi, K. Kyutoku, Y. Sekiguchi, M. Shibata, K. Taniguchi, *Phys. Rev.* **D96**(8), 084060 (2017). DOI 10.1103/PhysRevD.96.084060
266. F. Foucart, et al., *Phys. Rev.* **D99**(4), 044008 (2019). DOI 10.1103/PhysRevD.99.044008
267. D. Radice, A. Perego, K. Hotokezaka, S.A. Fromm, S. Bernuzzi, L.F. Roberts. Binary Neutron Star Mergers: Mass Ejection, Electromagnetic Counterparts, and Nucleosynthesis (2019). DOI 10.5281/zenodo.3588344. URL <https://doi.org/10.5281/zenodo.3588344>